Universitá di Napoli "Federico II"

SCUOLA POLITECNICA DELLE SCIENZE DI BASE
Laurea Magistrale in Ingegneria Aerospaziale

Master thesis

Wind tunnel testing on the aerodynamics of the directional control surface of a generic regional transport airplane

Candidate:
Vincenzo Dezio
Matricola M53000537

Thesis advisor:
Prof. Eng. Fabrizio Nicolosi

Research supervisor:
Dr. Eng. Danilo Ciliberti

Academic year 2016–2017

« Le vent se lève!...
il faut tenter de vivre »

Abstract

Previous works have shown that semi-empirical methods, mainly used in aircraf preliminary design and performance analysis, underestmates the effectveness of short aspect rato control surfaces, i.e. the aircraf directonal rudder. The purpose of this thesis is the experimental investgaton of a modular vertcal tail model in the wind tunnel of our department to estmate the effectveness of the rudder and to provide data about aerodynamics interference among airplane components concerning directonal control. Three vertcal tails are provided: all of them have the same geometrical characteristcs except for the rudder chord ratio, that is constant along the span but different for each model, in additon the models have two different aspect ratos with the possibility to change the rudder span for the tails with the higher aspect rato. These tails are mounted on a modular model of a generic regional turboprop aircraf designed and realized by our department in the previous years. The experimental tests campaign has been performed in the main subsonic wind tunnel facility of the DII. The results were collected from 48 confguratons (a total of 300 runs). The vertcal tail effectveness and the directonal control derivatve have been analyzed to changes of greater importance geometric parameters, plus the effects due to the aerodynamic interference of fuselage, wing, and horizontal tail. Results agree with data of previous numerical and experimental analyses, conferming that the applicaton of semi-empirical methods may oversize the vertcal tail in preliminary design phase. Results data also served to develop a new method to evaluate vertcal tail efectveness and rudder control power.

Contents

List of Figures

List of Tables

Chapter 1

Introduction

1.1 Phenomenology

When the flight path of an airplane no longer lies in its plane of symmetry, the relative wind will be making a certain angle to the airplane's center line, which will be referred to as the angle of sideslip, β, and it is assumed to be positive in sign when the relative wind strikes on pilot's right.

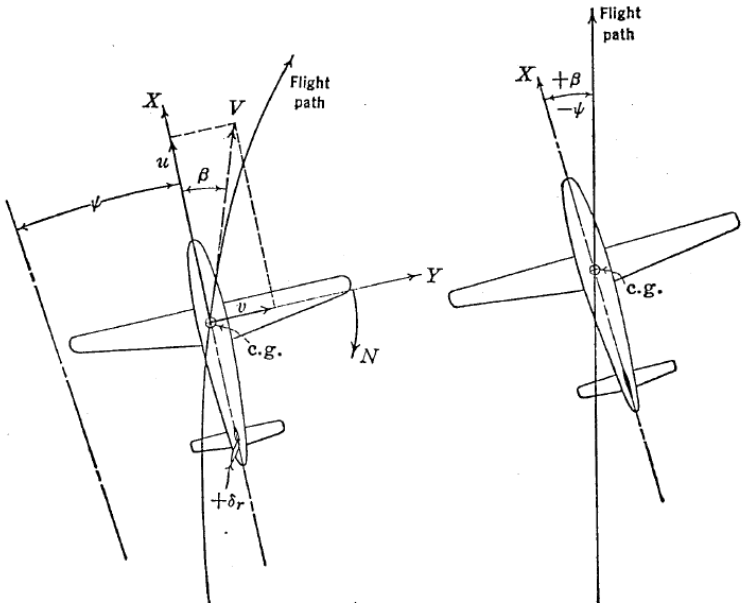

Figure 1.1 Asymetrical flight notation (left) - The straight slip (right).

The angle of sideslip, β, is equal to $\sin^{-1}(v/\mathrm{V})$ or for the small angles encountered in normal flight $\beta = v/\mathrm{V}$. It has to be noticed that the angle of yaw, ψ, defined as the angular displacement of the airplane's center line from some azimuth direction taken as zero at some given instant of time, differs from β in curved flight

paths while it's equal in magnitude but opposite in sign to it when a straight path is mantained, as shown in the figure 1.1.

Sideslip can help out during flight with asymmetric power or may be useful to accomplish some acrobatics, but in almost all flight conditions it is advantageous to mantein zero sideslip. The problem of directional stability and control is to ensure that the airplane will tend to remain in equilibrium at zero sideslip and to provide a control to mantein zero sideslip during maneuvers that introduce moments tending to produce sideslip [1].

1.2 Static Directional Stability

1.2.1 Stick-fixed directional stability

The static directional stability of an airplane is its tendency to develop restoring moments when distrurbed from its equilibrium angle of sideslip, usually taken as zero, then the static problem becomes the study of yawing moments developed by the airplane because of sideslip or yaw and their tendency to increase or decrease β.

The yawing moment coefficient will be discussed instead of the dimensional correspondent moment, this coefficient is obtained by dividing the yawing moment by the dinamic pressure q, the wing area S_{w} and the wing span b.

$$C_{\mathcal{N}} = \frac{\mathcal{N}}{qS_{\mathrm{w}}b} \tag{1.1}$$

The directional stability of the airplane can be assessed if a curve of the yawing moment coefficient, $C_{\mathcal{N}}$, with the angle of sideslip, β, (or of yaw, ψ) is obtained for any given airplane: a positive (or a negative) slope of this curve is required for the static directional stability. Hereafter it will be referred to ψ, so then the derivative $dC_{\mathcal{N}}/d\psi$ will be given in the short-hand notation $C_{\mathcal{N}_\psi}$ and will be given for degree.

A typical stable and unstable directional curve is shown in the figure 1.2, it is built up from contributions of many airplane's component parts, each of which produces yawing moments when flying at angles of sideslip: in order to obtain the final variation analytically, tha magnitude of the contributions from the major components must be developed analytically and then summed up.

Wing's contribution to the directional stability of the airplane is very small, the factor that affects the most is its angle of sweep, Λ: swept-back wings have slight directional stability while swept-forward wings are slightly unstable, straight wings' contribution is almost negligible in comparison to other airplane's parts.

This small contribution from the swept wing can be estimated to a first approximation from the following formula:

$$(C_{\mathcal{N}_\psi})_{\mathrm{wing}} = -.00006(\Lambda^\circ)^{\frac{1}{2}} \tag{1.2}$$

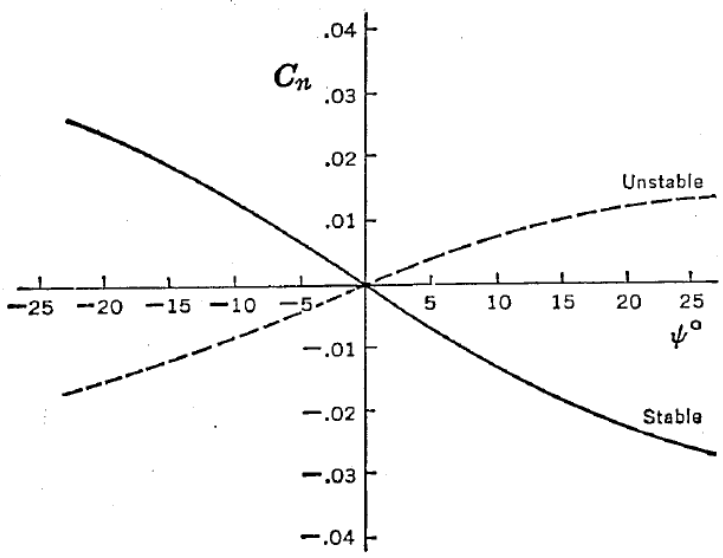

Figure 1.2 Typical wind-tunnel curves C_N versus ψ.

where Λ is the sweep angle of the quarter chord in degrees.

Fuselage's contribution to the directional stability is usually unstable and one of the major effects. Assuming that a fuselage is a slender body of revolution, when it is placed in a potential flow field at a certain angle of attack the pressure is distributed as shown in the figure 1.3: net pressure drag is zero, net lift is zero, net pitching moment is positive and unstable. It is a function of the dynamic pressure, q, and the volume of the fuselage as demonstrated by Munk in 1923, who also established a correction factor (that depends on the fuselage fineness ratio L/D). The yawing moment due to the angle of sideslip then is exactly the same and is even easier to estimate than the pitching moment thanks to the fact that the wing does not disturb the sideslip angle.

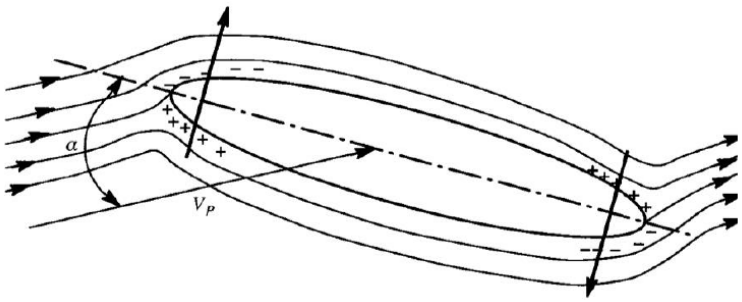

Figure 1.3 A body of revolution in a potential flow at a certain angle of attack.

The fuselage gives a large unstable contribution for conventional airplane con-

figuration that varies from .006 to .0012. Many empirical approaches have been made to estimate this yawing moment and one of the best was developed during World War II, here follows the formula:

$$(C_{N_\psi})_{\text{fus}} = \frac{.96K_\beta}{57.3}\left(\frac{S_s}{S_w}\right)\left(\frac{L_f}{b}\right)\left(\frac{h_1}{h_2}\right)^{1/2}\left(\frac{w_2}{w_1}\right)^{1/3} \tag{1.3}$$

where S_s is the projected side area of the fuselage, L_f is its over-all length and the coefficients h_1, h_2, w_1, w_2 can be obtained by reffering to the sketch in the figure 1.4. The values of the empirical constant K_β are given still in the figure 1.4 as functions of the fineness ratio, L_f/h and the location of the c.g. on the body, d/L_f.

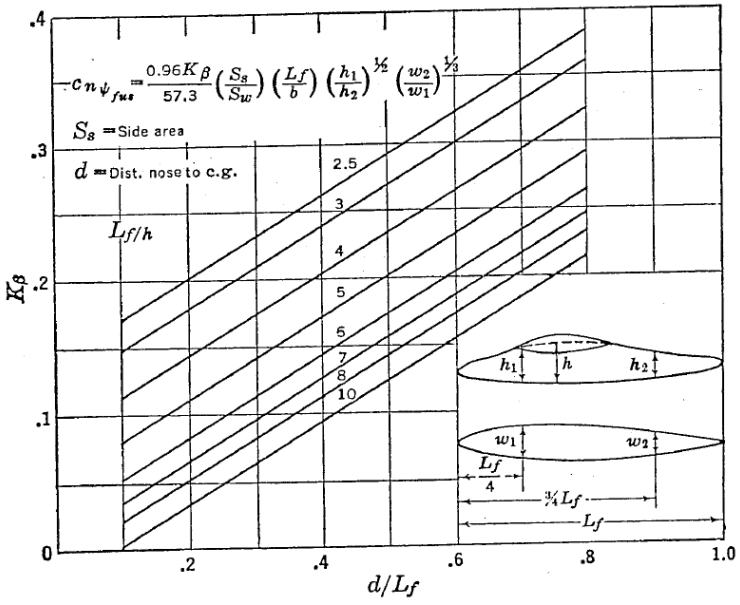

Figure 1.4 Fuselage directional stability coefficient.

When the contributions of wing and fuselage are combined the final value may differ for different configuration of wing's positioning, this interference is usually slightly stabilizing but it is never larger than $\Delta_1(C_{N_\psi}) = -.0002$ for high wing configuration, while is almost zero for a low wing.

Propeller's contribution to the directional stability can have large effects, destabilizing if a tractor and stabilizing if a pusher propeller. It arises from the side force component at the propeller disk created because of yaw.

The yawing moment coefficient produced by this force is:

$$C_N = \frac{Y_p \times l_p}{qS_w b} \tag{1.4}$$

where the cross wind force, expressed in terms of its coefficient, is $C_{Y_p} = Y_p/q(\pi D^2/4)$. The stability contribution of the running propeller can be obtained by differentiating

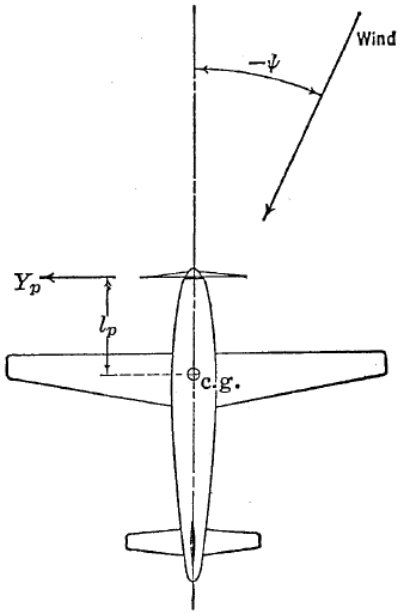

Figure 1.5 Propeller side force moment.

the 1.4 respect to ψ in degrees, so that the final formula is:

$$C_{N_\psi} = \frac{\pi D^2 l_p \left(\frac{dC_{Y_p}}{d\psi}\right) N}{4 S_w b} \tag{1.5}$$

where N is the number of propellers. The derivative $dC_{Y_p}/d\psi$ depends on the characteristic of the propeller (number of blades, blade angle, etc.) and can be estimated from propeller data in literature.
By now the total value of the directional stability is as follows:

$$(C_{N_\psi})_{\text{Airplane}} = (C_{N_\psi})_{\text{Wing}} + (C_{N_\psi})_{\text{Fus}} + (C_{N_\psi})_{\text{Prop}} + \Delta_1 (C_{N_\psi}) \tag{1.6}$$

this summation usually gives a directionally unstable airplane. However an airplane with only these components can be made stable: a pure flying wing type airplane (no fuselage) with swept-back wings and pusher propellers will be directionally stable without any additional stabilizing surfaces. In the conventional airplane anyway the overall directional stability is unstable, then an additional stabilizing surface must be incorporated not only to overcome the instability of the other components but also to give the desidered level of directional stability. This surface is the normal vertical tail placed as far from the c.g. as possible.

Vertical tail's contribution to the directional stability can be computed considering the yawing moment produced as the lift created on the vertical tail at some

angle of yaw, L_v multiplied by the arm from the aerodinamic center or the vertical tail to the airplane's c.g., l_v. In terms of the yawing moment coefficient:

$$C_N = -\left(\frac{dC_L}{d\psi}\right)_v \psi \frac{S_v}{S_w}\frac{l_v}{b}\frac{q_v}{q} \tag{1.7}$$

usually the term $\frac{S_v}{S_w}\frac{l_v}{b}$ is indicated as the vertical tail volume coefficient, V_v, and the term $\frac{q_v}{q}$ as the dynamic pressur ratio, η_v. The coefficient C_{L_v} can be expressed as

$$C_{L_v} = a_v(\alpha_v + \tau_v\delta_r) = a_v\alpha_v \tag{1.8}$$

where δ_r=0 because of the stick-fixed condition, but the derivative $dC_{L_v}/d\psi$ is not exactly the slope of vertical plane's lift curve, a_v, because of the sidewash, σ, created by the wing-fuselage combination at an angle of yaw. Almost all of the sidewash comes from the fuselage that exhibits a behaviour similar to a cylinder in an airflow: destabilizing the flow in the airstream beside the fuselage and stabilizing the air above it. The wing interference is linked to the vortex sheet as a result of the inboard motion of the air above the vortex sheet and outboard motion of the flow below it. As result a low-wing airplane shows a stabilizing effect due to the sidewash, whereas a high-wing design should have a very small sidewash influence. Therefore the following substitution can be done.

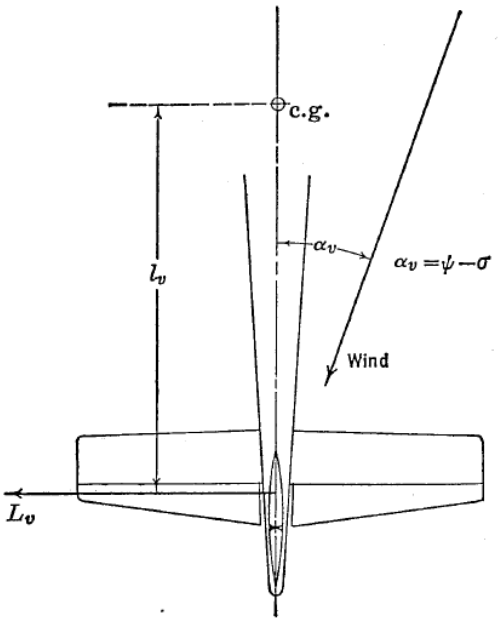

Figure 1.6 Yawing moment of vertical tail.

$$\alpha_v = \psi - \sigma \tag{1.9}$$

$$\frac{d\alpha_v}{d\psi} = 1 - \frac{d\sigma}{d\psi} \tag{1.10}$$

$$C_{\mathcal{N}} = -a_v \left(1 - \frac{d\sigma}{d\psi}\right) \psi V_v \eta_v \tag{1.11}$$

$$C_{\mathcal{N}_\psi} = -a_v \left(1 - \frac{d\sigma}{d\psi}\right) V_v \eta_v \tag{1.12}$$

This last expression can be broken as follows.

$$C_{\mathcal{N}_\psi} = -a_v V_v \eta_v + a_v \frac{d\sigma}{d\psi} V_v \eta_v \tag{1.13}$$

$$C_{\mathcal{N}_\psi} = (C_{\mathcal{N}_\psi})_v + \Delta_2 C_{\mathcal{N}_\psi} \tag{1.14}$$

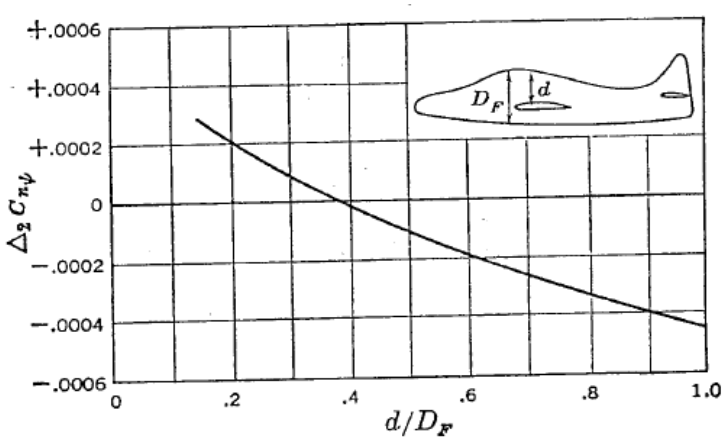

Figure 1.7 Interference correction to $C_{\mathcal{N}_\psi}$.

The term $\Delta_2 C_{\mathcal{N}_\psi}$ is that part of contribution that arises from the sidewash, an estimate of this factor can be obtained from the curve given in the figure 1.7: as stated before a low-wing configuration gives a stabilizing effect while for an high-wing it can even change in sign and gives a destabilizing effect. The slope of the vertical tail's lift curve is a function of the effective aspect ratio of the vertical tail, $\mathcal{AR}_{e_v}$. It is greater than the geometrical aspect ratio because of the end plate effect of the horizontal tail: the relative size and position of the two tails modify the aspect ratio, in particular the effect is bigger for a T-tail configuration and it increases for increasing values of the tails surface ratio, S_h/S_v. It can be estimated as follows.

$$\mathcal{AR}_{e_v} = 1.55 \frac{b_v^2}{S_v} \tag{1.15}$$

The final estimate of the directional stability coefficient can be obtained from the summation of the different factors discussed before.

$$(C_{\mathcal{N}_\psi})_{\text{Airplane}} = (C_{\mathcal{N}_\psi})_{\text{Wing}} + (C_{\mathcal{N}_\psi})_{\text{Fus}} + (C_{\mathcal{N}_\psi})_{\text{Prop}} + (C_{\mathcal{N}_\psi})_{\text{v}} + \Delta_1 (C_{\mathcal{N}_\psi}) + \Delta_2 C_{\mathcal{N}_\psi} \tag{1.16}$$

The desirable level of directional stability is difficult to express in general terms, for conventional airplane configuration a good level is between -.0015 and -.0020, anyway the following formula is suggested.

$$(C_{N_\psi})_{\text{desirable}} = -.0005 \left(\frac{W}{b^2}\right)^{1/2} \tag{1.17}$$

1.2.2 Stick-free directional stability

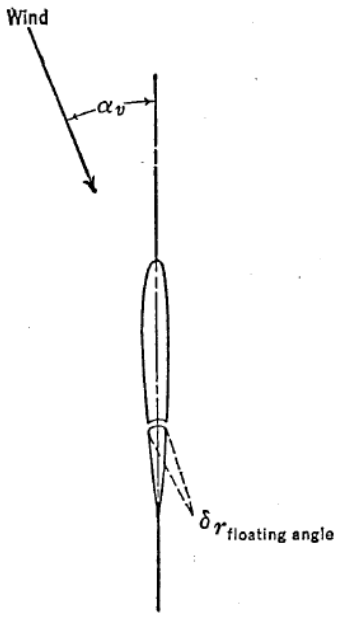

Figure 1.8 The floating rudder.

When the rudder is left free to float it can have large effects on the directional stability of the airplane: the restoring moment due to the vertical tail will be decreased if the rudder floats with the wind and will be increased if the rudder floats against it. The floating angle can be expressed analitically:

$$\delta_{r_{\text{float}}} = -\frac{C_{h_\alpha}}{C_{h_{\delta_r}}} \alpha_v \tag{1.18}$$

this angle changes the effective incidence angle of the vertical tail.

$$(\alpha_v)_{\text{eff}} = \psi - \sigma + \tau_v \delta_{r_{\text{float}}} \tag{1.19}$$

where σ is the sidewash angle, i.e. the deviation angle of the flow given by the interference between the wing and the fuselage which arises in a laterally diverted flow conditions ($\beta > 0$), similarly to the downwash in the longitudinal case at $\alpha >$

0; τ is the rudder's effectiveness defined as $\mathrm{d}\alpha/\mathrm{d}\delta$, see section 1.3. The stability contribution of the vertical tail with a free rudder is therefore:

$$C_{\mathcal{N}} = -a_v(\psi - \sigma + \tau_v \delta_{r_{\text{float}}})V_v\eta_v = -a_v\left(\psi - \sigma + \tau_v \frac{C_{h_\alpha}}{C_{h_{\delta_r}}}\psi\right)V_v\eta_v \tag{1.20}$$

$$(C_{\mathcal{N}_\psi}) = -a_v\left(1 - \tau_v \frac{C_{h_\alpha}}{C_{h_{\delta_r}}}\right)V_v\eta_v + \Delta_2 C_{\mathcal{N}_\psi} \tag{1.21}$$

The stick-free directional stability of the airplane is made manifest to the pilot by the pedal force required to produce the balancing value of δ_r: if the gradient is too low it is very difficult for the pilot to hold zero sideslip during maneuvers, if it is too high the airplane will feel stiff directionally to the pilot. The equation for the pedal force, PF, is given by the product of the mechanical gearing, G, and the rudder hinge moment:

$$PF = G \times HM = G(C_{h_\alpha}\psi + C_{h_{\delta_r}}\delta_r + C_{h_{\delta_t}}\delta_t)q\eta_v S_r c_r \tag{1.22}$$

The rudder angle can be expressed as follow

$$\delta_r = \frac{d\delta_r}{d\psi}\psi \tag{1.23}$$

where

$$\frac{d\delta_r}{d\psi} = -\frac{(C_{\mathcal{N}_\psi})_{fixed}}{C_{\mathcal{N}_{\delta_r}}} \tag{1.24}$$

Substituting 1.24 in the 1.22

$$PF = Gq\eta_v S_r c_r\left[C_{h_\alpha}\psi - C_{h_{\delta_r}}\frac{(C_{\mathcal{N}_\psi})_{fixed}}{C_{\mathcal{N}_{\delta_r}}}\psi + C_{h_{\delta_t}}\delta_t\right] \tag{1.25}$$

differentiating respect to ψ and rearranging

$$\frac{dPF}{d\psi} = -\frac{Gq\eta_v S_r c_r C_{h_{\delta_r}}}{C_{\mathcal{N}_{\delta_r}}}(C_{\mathcal{N}_\psi})_{\text{free}} \tag{1.26}$$

The 1.26 holds only for linear hinge moment variation and constant directional stability, true for ± 10 degrees of sideslip or rudder deflection. At high angle of sideslip the rudder starts to float over rapidly with increase in sideslip, this condition becomes accentuated if the vertical tail begins to stall due to the depression that develops in the downwind part of the rudder.

A typical curve of the floating angle versus the yaw is shown in the figure 1.9, the tendency of the rudder to float rapidly at high angles of sideslip leads to the phenomenon known as rudder lock. Considering that the rudder angle required varies linearly, the pedal force is a function of the difference between the two curves. At high angles of yaw the floating angle may catch up with the required rudder angle at which point the pedal force will be zero. If the sideslip is increased beyond this

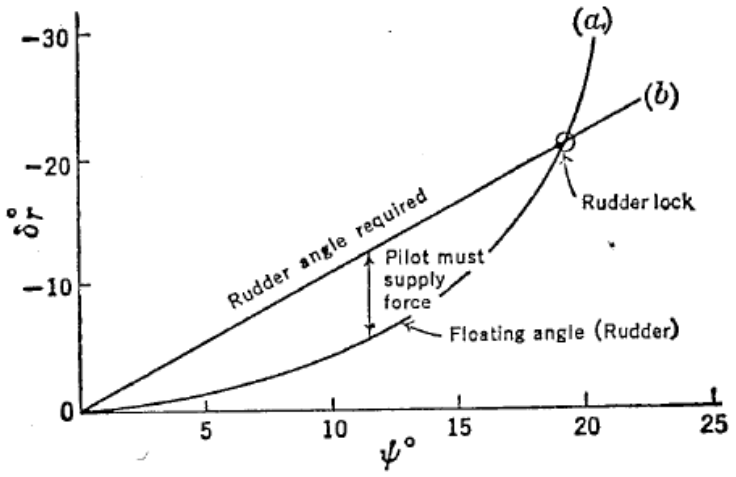

Figure 1.9 Rudder lock.

point, the pedal force will reverse and the rudder will continue to deflect up to its maximum value.

A way out of the rudder lock problem is the addition of a dorsal fin: a small surface extension installed at the leading edge of the vertical tail's root. It gives two advantages: it increases the fuselage stability at high angles of sideslip and it reduces the tendency of the vertical tail to stall, the increase in directional stability will require more rudder angle δ_r for trim and reduce the redder lock possibilities. A typical example of dorsal fin's effect on the pedal force versus sideslip characteristics is shown in figure 1.10. More insights on the dorsal fin aerodynamics and design can be found in [2].

1.3 Directional control

There are many flight conditions or maneuvers that introduce yawing moments, these must be opposed by some yawing moment of control in order to keep the zero sideslip condition. This control moment is supplied by the pilot through the deflection of a rudder that is assumed positive if the trailing edge is rotated to the left looking the aircraft from behind. This deflection produces a lateral force to the right that gives a negative yawing moment, therefore the control power:

$$C_{\mathcal{N}_{\delta_r}} < 0 \tag{1.27}$$

An expression for the rudder control power can be developed starting from the expression of the yawing moment due to a deflection of the rudder, δ_r:

$$\mathcal{N} = -L_v \times l_v \tag{1.28}$$

$$C_{\mathcal{N}} = -\left(\frac{dC_{\mathrm{L}}}{d\delta_r}\right)_v \delta_r V_v \eta_v \tag{1.29}$$

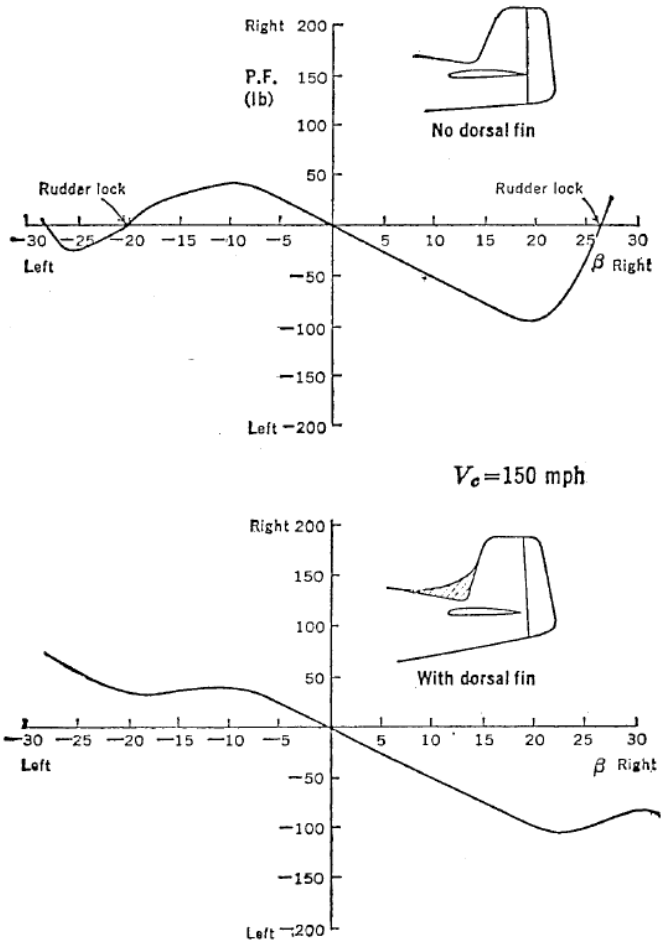

Figure 1.10 Effect of the dorsal fin.

$$\left(\frac{dC_{\mathrm{L}}}{d\delta_r}\right)_v = \frac{dC_{\mathrm{L}}}{d\alpha_v}\frac{d\alpha_v}{d\delta_r} = a_v\tau_v \tag{1.30}$$

where τ_v (= $d\alpha_v/d\delta_r$) indicates how many degrees of rudder deflection are needed to obtain one angle of attack α_v, from which it takes the name of rudder efficiency. The rate change of yawing moment coefficient per degree change in rudder angle is obtained from the second of these equations by differentiating it respect to δ_r.

$$C_{N_{\delta r}} = \frac{dC_N}{d\delta_r} = -a_v\tau_v V_v\eta_v \tag{1.31}$$

Rudder control power varies considerably between airplanes but a good mean value is assumable equal to $C_{N_{\delta r}}$ = -.001, then if the directional stability is at the same level of C_{N_ψ} = -.001 it follows that 1 degree of rudder deflection can balance 1 degree of yaw. For most rudders, deflections are usually limited to plus or minus 25 or 30 degrees, but non-linear effects on $C_{N_{\delta r}}$ begin from δ_r = 15 degrees, which

lead to the decrease of the rudder efficacy τ_v. Typical wind tunnel tests for rudder effectiveness are shown in the figure 1.11.

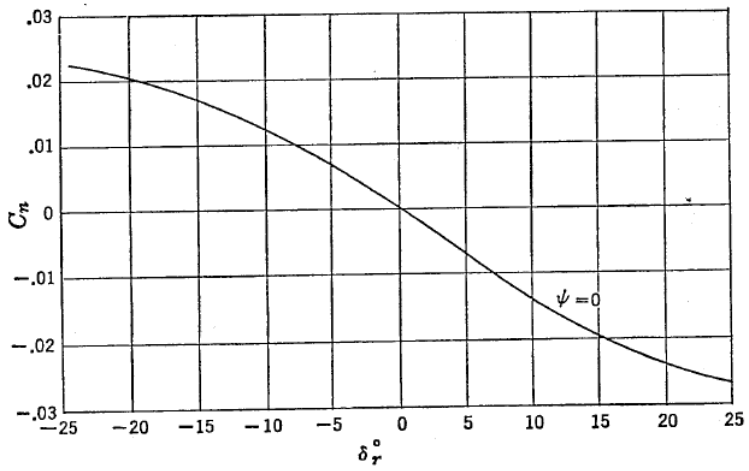

Figure 1.11 Rudder power.

The flight conditions or maneuvers that introduce yawing moments that must be overcome by the rudder control and that marks the most critical condition to size the vertical plane are the following:

a. *Adverse yaw* - When the ariplane is rolled into a turn, the rolling control together with the inclination of the lift vectors on the rolling wing creates yawing moments that will produce sideslip, critical conditions are at high lift coefficient (low speed) with full rolling control.

b. *Slipstream rotation* - For single-engine airplanes, the slipestream behind the propeller has a rotational component which changes the vertical tail's angle of incidence, critical conditions are for high power at low speed.

c. *Cross wind during take-offs and landings* - The rudder should be able to hold the sideslip required to make take-offs and landings during cross wind at least to speeds 1.2 of the stalling speed, below this value brakes can be used.

d. *Spinning* - Spins can be entered intentionally or unintentionally, from any flight attitude if the aircraft has sufficient yaw while it is at the stall point, this cause the aircraft to autorotate (yaw) toward the more deep stalled wing due to its higher drag and loss of lift: in most cases the rudder control os the major recovery control.

e. *Antisymmetric Power* - In multiengined aircraft the failure of one engine at low airspeeds (critical condition at the minimum control speed) will create a heavy yawing moment that must be overcome by the rudder: this is nearly always the design condition for these airplanes.

The rudder control power required to overcome the adverse yaw during a rolling manouver is usually not very high and not often designs the rudder. Spinning requirements are not critical respect to others and slipestream ones are for single-engine aircraft, so then the most critical conditions to size the vertical tail are the antisymmetric power and the cross wind during take-offs and landings.

As stated before, on multi-engine airplanes if a failure occurs to one of the engines it is required that the rudder must be powerful enough to balance the yawing moment produced by the operative engine (a contribution from the increased drug of the failed engine should be considered too). Regulations state that such a maneuver can be performed with a maximum bank angle ϕ, a rotation about the aircraft longitudinal axis, of 5 degrees to compensate the drift of the aircraft that arises because of the lateral force and that a residual sideslip angle β of 5 degrees is accepted, anyway in the design phase it can be assumed equal to zero: this is a conservative consideration since the residual β introduces an additional yawing moment due to the directional stability that helps to control the aircraft in such conditions.

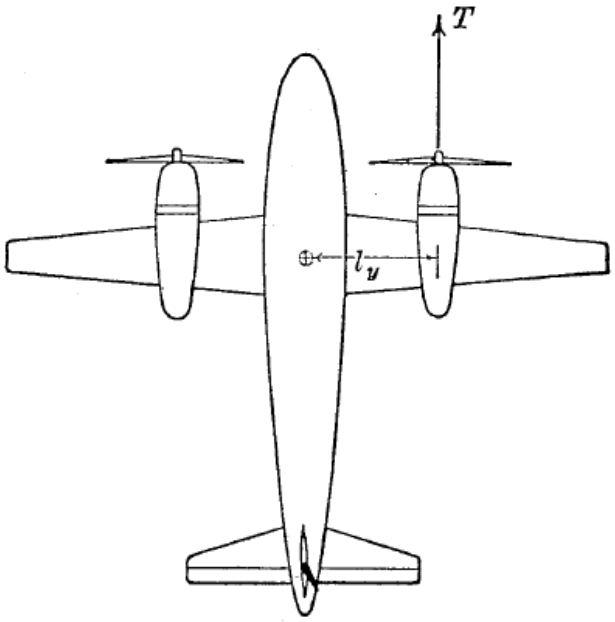

Figure 1.12 Yawing moment due to antisymmetric power.

The yawing moment provided by the operative engine is equal to:

$$\mathcal{N} = T \times l_T \tag{1.32}$$

while the one produced by the rudder is given by the eq. 1.28. The general equilibrium expression in such conditions is:

$$C_{\mathcal{N}} = C_{\mathcal{N}_T} T + C_{\mathcal{N}_{\delta_r}} \delta_r + C_{\mathcal{N}_{\delta_a}} \delta_a = 0 \tag{1.33}$$

where $C_{N_{\delta_a}}$ is the coupling between lateral and directional motions, that can be neglected placing $\delta_a = 0$ (so $\delta_r = \delta_{r_{\max}}$), and C_{N_T} is the yawing moment coefficient due to the antisymmetric power and has this expression:

$$C_{N_T} = \frac{375BHP\eta_p l_y}{VqS_w b} \tag{1.34}$$

where V is in mph. It is a function of $1/V^3$ while from equation 1.31 it can be seen that $C_{N_{\delta_r}}$ is indipendent from speed, plotting then these two coefficients versus the speed it is possible to find the minimum value of V for which the control is still guaranteed, the minimum control speed V_{MC}, as shown in the figure 1.13. It is possible

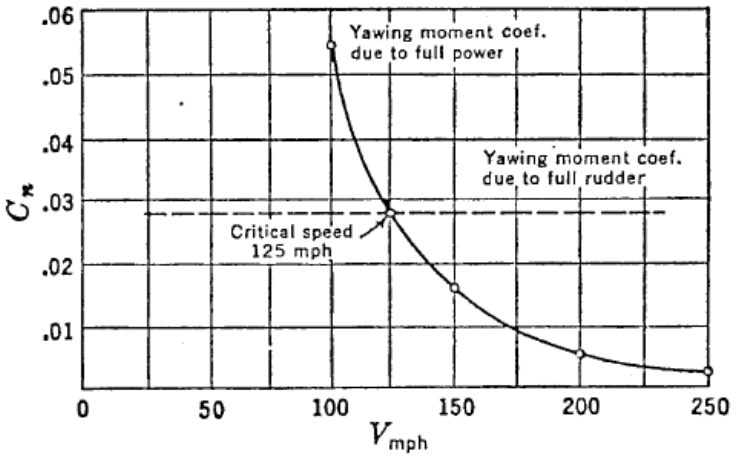

Figure 1.13 Critical speed due to antisymmetric power.

to notice that increasing the vertical tail's surface S_v drives up the C_N due to rudder deflection obtaining intersection with the other curve to a lower speed. Regulations state that V_{MC} must be down to 1.2 times the airplane's stalling speed in the take-off configuration, therefore, if this statement is not respected, it is necessary to re-size the vertical tail. However a bigger S_v has its considerable disadvantages, including increased costs and weight, with the consequential affects on the gravity center position and the static longitudinal margin, in addition it gives greater wetted area that implies an increase of the parasite drag and a reduced maximum airspeed: it is necessary so to optimize the sizing of the vertical tail. A final note is for propelled aircraft, the V_{MC} obtained from flight tests is different depending on the engine that goes into failure because of the different effects produced on the vertical tail by the sense of rotation of the propellers: in this case the critical engine is the one responsable for a greater V_{MC} and in the preliminary design phase is the one analyzed.

As regards to the landing during cross wind condition (more critical then the take off) it is necessary that the rudder is able to balance the yawing moment caused by the wind in order to mantain the desired flight path. The equilibrium equation

in this condition, assuming that the propulsive effects and the contribution due to the aileron deflection (sideslip generates a rolling moment because of the dihedral effect) are negligible, is the following:

$$C_N = C_{N_{\delta_r}} \delta_r + C_{N_\beta} \beta = 0 \tag{1.35}$$

It has to be guaranteed that with a maximum rudder deflection of 20-25 degrees it is possible to balance not less than 16-18 degrees of sideslip, taking into account the non-linear effects on the stability derivative C_{N_β} and the control power $C_{N_{\delta_r}}$. The first derivative's non-linear effects are the behavior of the fuselage and the stall of the vertical tail at high values of the sideslip that can be reduced by mean of a dorsal fin, while the non-linear effects on the control power are due to the reduction of the rudder effectiveness τ_v at high angle of rudder deflections δ_r that can be modified managing the chord ratio c_r/c_v (rudder chord and aerodynamic chord of the vertical tail respectively).

1.4 Scope of the work

The purpose of this thesis is the wind tunnel experimental investigation of control surfaces for wing with short aspect ratio, in particular focusing on the estimation of the effectiveness τ of a vertical tail's rudder for the directional control of a generic regional transport airplane, and to provide data about aerodynamics interference among airplanes components for different configurations in sideslip condition.

Comparisons between semi-empirical methods, numerical calculations and wind tunnel experimentations have already been performed by the DAF research group, Dept. of Industrial Engineering of the University of Naples "Federico II" and have shown discrepancies in the results about aircraft control surface effectiveness estimation.

In particular, part of the work in [3] was focused on the evaluation of control surface effectiveness on several geometries of horizontal and vertical tails (with and without dorsal fin), see Figure 1.15.

Figure 1.14 shows the close agreement between numerical and experimental results for the P2012 vertical tail, while the semi-empirical method underestimates the rudder effectiveness expecially at high angles of rudder deflection δ_r.

The subsequent researches carried out by the team allowed to implement a new method for the calculation of the rudder effectiveness, part of this work is to validate this method and to provide insights on the aerodynamics of the directional control surface.

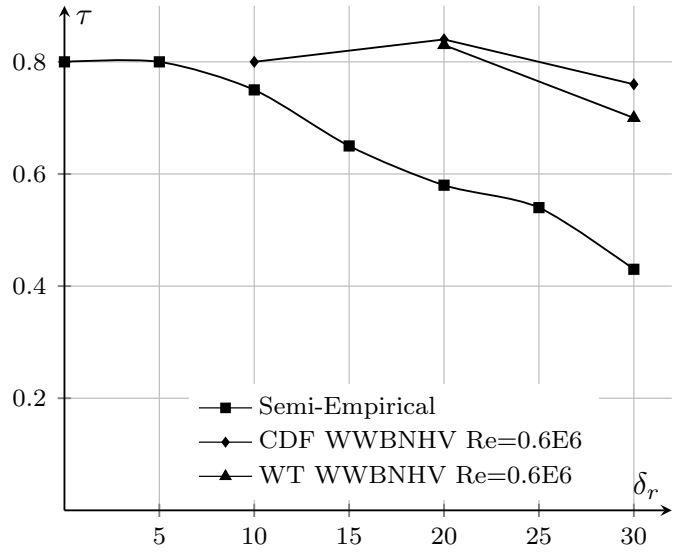

Figure 1.14 Comparison between numerical, semi-empirical and wind tunnel tests results in terms of rudder effectiveness τ.

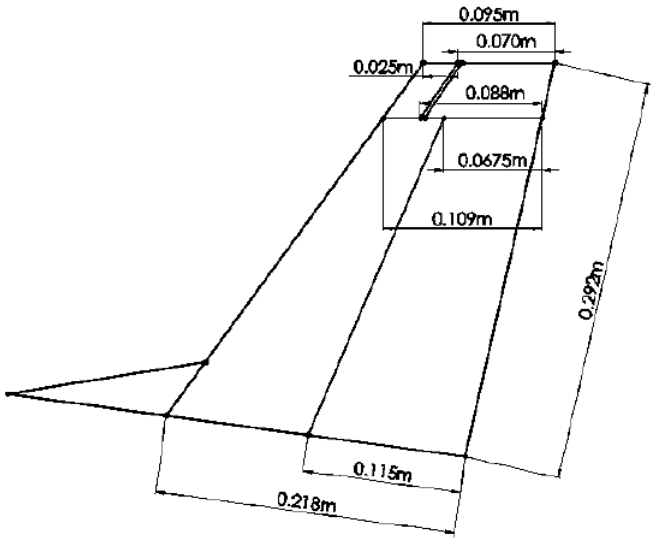

Figure 1.15 Tecnam P2012 vertical tailplane [3].

Chapter 2

The experimental modular model

2.1 Vertical tail design

Tail surfaces sizing and shaping is almost exclusively determined by stability and control considerations. A vertical tail, which provides *directional* stability and control, is usually made up of two parts: a fixed wing that provides the stability, called *stabilizer*, and a plain flap, the *rudder*, that is the control surface (Figure 2.1). Here follows a list of the most typical shapes for a tail, some of them are shown in the figure 2.2 [4].

- In a *standard* configuration roots of both horizontal and vertical tail are attached directly to the fuselage, this is the most convenient shape structurally. The aerodynamic interference with the fuselage and the horizontal tail increases the effectiveness of the vertical surface, however large areas of the tails are affected by the converging flow of the fuselage, which can locally decrease the dynamic pressure.

- In a *T-tail* configuration the horizontal tail is mounted on the tip of the vertical surface, keeping it away from the engine exhaust and reducing the

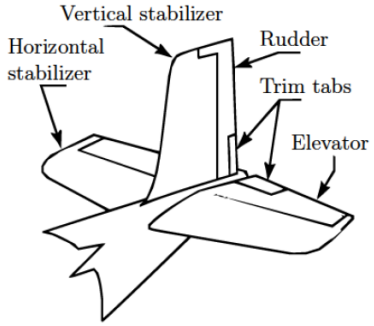

Figure 2.1 Tail components definition.

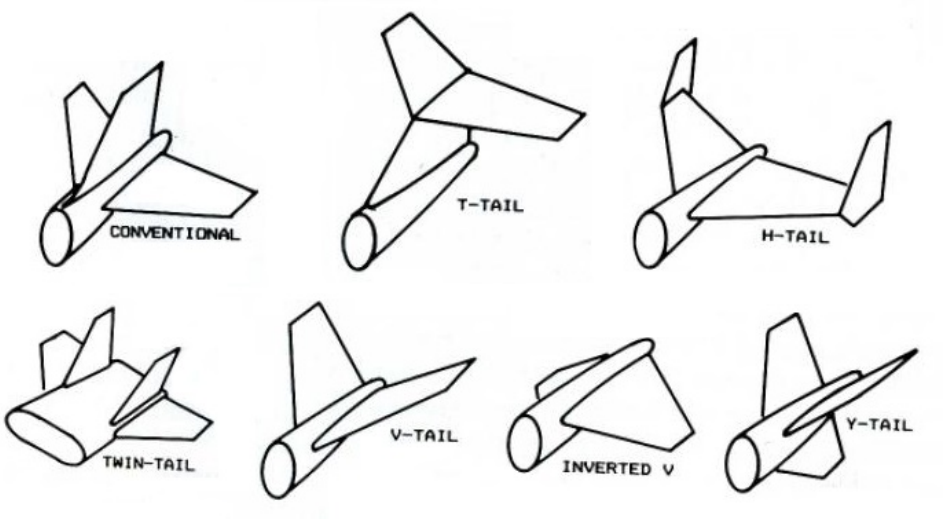

Figure 2.2 Tails configurations.

aerodynamic interference. The vertical tail is in its most effective configuration since the horizontal tail acts as an end-plate, however disadvantages include increased tail aerodynamic loads, potential flutter problems and wing deep-stall.

- In a *H-tail* or *twin* configuration two vertical surfaces are mounted on the horizontal tail's tips and act as end-plates increasing its effectiveness. The increased number of vertical surfaces reduces tail span and the distance from the fuselage keeps them out of fuselage's flow at high angles of attack, greatly increasing the maneuverability of the aircraft. Complex control linkages and reduced ground clearence discourage their more widespread use.

- A *V-tail* configuration combines functions of horizontal and vertical tails, the main purpose is to reduce the wet surface and then the parassite drug, more over it is sometimes chosen because of its increased ground clearence. However it requires mixing of rudder and elevator controls and usually often exhibits reduced control in combined yaw and pitch maneuvers, an inverted *V-tail* can avoid this effect but needs taller gears.

- A *Y-tail* configuration is quite similar to a V type with the addiction of a little vertical surface for the directional control. This shape has been used when the downward projecting vertical surface can serve to protect a pusher propeller from ground strikes, while on the F-4 an inverted *Y-tail* has been used to keep the horizontal tail out of the wing's flow for high angles of attack. In both cases taller gears are required.

Design of vertical tailplanes depends on the type of airplane (and so the flow regime), engine numbers and position, wing-fuselage and horizontal tail position:

all these factors affect the stability derivatives, i.e. the variation of aerodynamic coefficients with the indipendent variable β; in addition design requirements are often set by extreme flight conditions as stated in the section 1.3, like minimum control speed with one engine inoperative or maximum cross-wind capability. The following design requirements can be formulated for vertical tailplanes: [5]

1. Equilibrium must be achieved in all flight conditions.

2. It must be provided a sufficiently contribution to static and dinamic stability, thus the sideforce derivative of the isolated vertical tail

$$C_{Y_{\beta,v}} = C_{L_{\alpha,v}} \frac{S_v}{S} \tag{2.1}$$

   has to be determined, its value depending on its lift curve slope and the relative size with respect to the wing. If a high lift gradient is desirable, the aspect ratio AR_v should be the largest possible with the minimum sweep angle Λ_v.

3. A sufficient control capability must be provided too, in addition control should be possible with acceptable control torque

$$\mathcal{M}_h = q_\infty C_h S_c \bar{c}_c \tag{2.2}$$

   which depends on control surface area S_c and chord $\bar{c}_c$ behind the hinge line, the dyamic pressure q_∞ and the hinge moment coefficient C_h.

4. The high angles of sideslip (up to 25 deg) that can be reached require low aspect ratio and sweep. Both delay the stall of the vertical tail, this is more serious when flying in possible icing conditions.

5. A high aspect ratio has an adverse effect on the weight, whereas for the taper ratio an excessive value may lead to premature tip stall while lowering the weight. Thus a compromise in high lift gradient and low aspect ratio and taper ratio must be considered.

2.2 Introduction to the model

The purpose of this thesis is the experimental investigation of a vertical tail model in the wind tunnel of our department to estimate the effectiveness τ (defined in 1.3) of the rudder and to provide data about aerodynamics interference among airplane components for different configurations in sideslip condition.

Three tails are provided (*A*, *B* and *C*): all of them have the same geometrical characteristics, reported in the table 2.1, except for the rudder chord ratio, c_r/c_v or c_r/c, that is constant along the span but different for each model (the rudder's chord is measured from the center of rotation placed in the hinge's center), in addition the models have two different aspect ratios $\mathcal{AR}$ for a total of six configurations. These tails are mounted on a model of a generic regional turboprop aircraft designed and realized by our department in the previous years. An in depth description of this model was reported by Ciliberti in [6], from now on we will refer to it as the aircraft model.

Figures 2.3 and 2.4 show two different section views: a plan form for both aspect ratios and the airfoil section of the three rudder's tip chord.

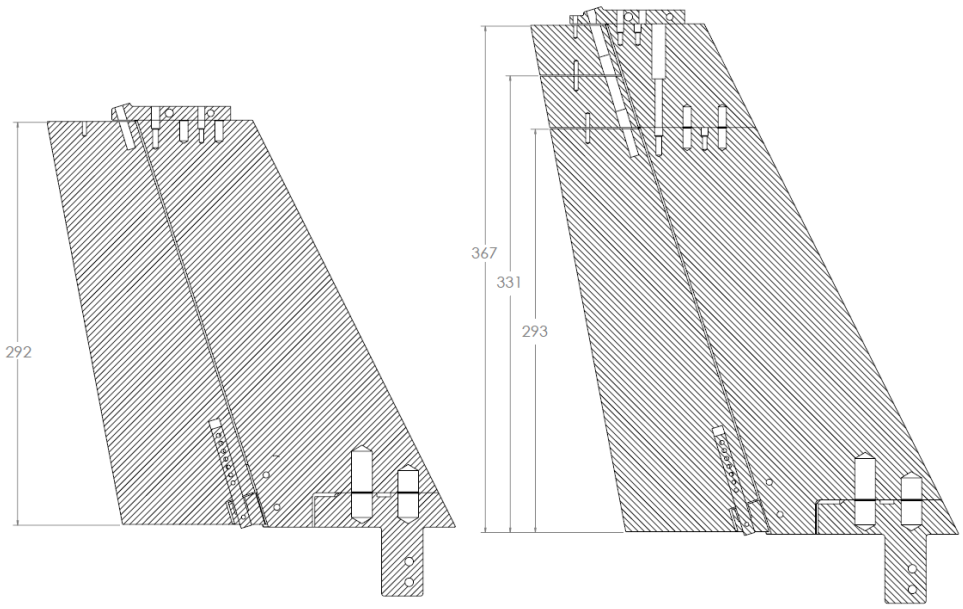

Figure 2.3 Section views of the model: the plan forms belong to the assembly *B* for $\mathcal{AR}$ = 1.5 (left) and $\mathcal{AR}$ = 2.0 (right).

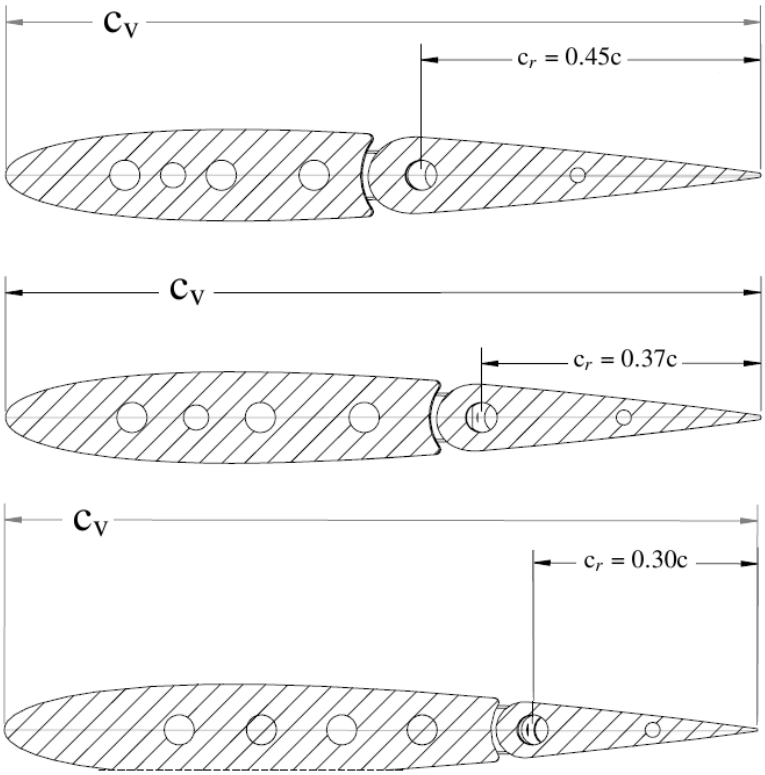

Figure 2.4 Section views of the model: the airfoils belong to the tip chords of each assembly.

Table 2.1 Main models geometrical characteristics.

	AR_1	AR_2
Value	1.5	2.0
c_{root}	0.241m	
c_{tip}	0.150 m	0.125 m
λ	0.62	0.52
c_{r_A}/c_v	0.45	
c_{r_B}/c_v	0.37	
c_{r_C}/c_v	0.30	
m.a.c.	0.200 m	0.190 m
full span, b_v	0.292 m	0.367 m
surface, S_v	0.058 m^2	0.068 m^2
tail arm, l_v	0.833 m	0.846 m
V_v ($S_v l_v/S_w b$)	0.146	0.174
Λ_{LE}	26.6 deg	
weight	2.9 Kg	3.2 Kg

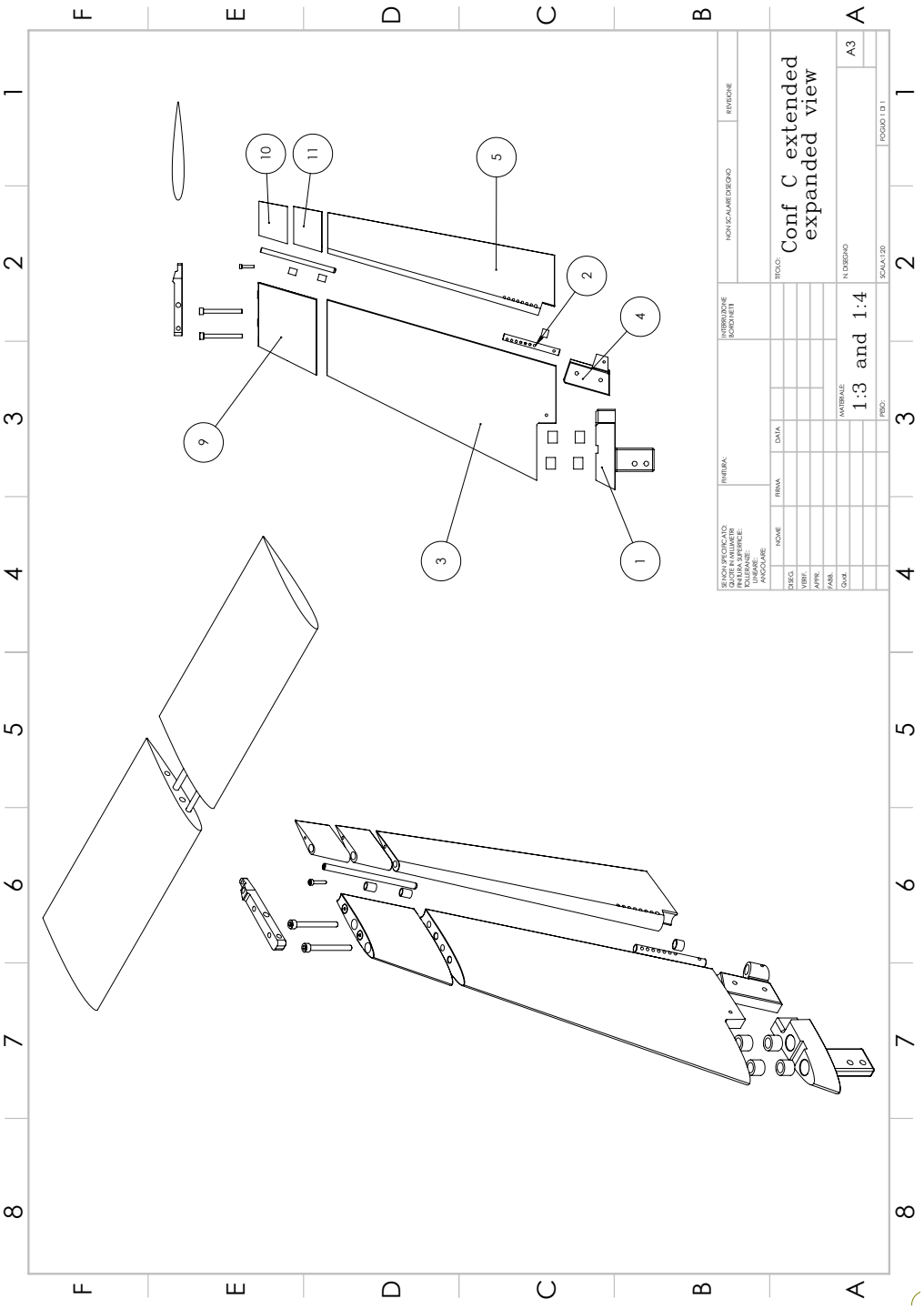

Figure 2.5 Exploded view of the vertical tail *C*.

Considering that all tails have the same assembly here follows a description of each component of the *C* configuration shown in the figure 2.5, the CAD models have been realized in aluminum alloy 2024-O with CNC milling by Eurotech sas. The CAD drawings of the main components are reported in A.

- №1 is the common base of the models because it is the only part all three of them have in common and on which they are mounted. It is fixed on the tail cone of the aircraft model by mean of a separate load cell, as shown in the figure 2.6.

Figure 2.6 The common base of the vertical tail assemblies mounted on the off-center load cell.

- №3, is the stabilizer that is directly inserted into the base. By mean of the №4 it is conected to the hinge, №2, that has seven holes set on a spiral allowing the rudder, №5, to have as many rudder deflections: these five components together make the vertical tail with $\mathcal{R}$= 1.5. The rudder is mounted on the hinge that acts as rotational axis.
  Rudder's range of excursion and the values of the intermediate angles δ_r are reported in table 2.2: it should be noted that the angle fixation is determined by a plug inserted between the hinge and the rudder, the attachment is secured by an additional grub screw at the base of the hinge too. However, the actual pairing of the parts presents clearence fits that, depending on the mounting, produce a real δ_r angle different from the design one. Therefore, several measures of the deflection angle have been repeated with a electronic level tool to determine the actual value of the angle at each spiral station. The actual angles' values are reported in the table 2.2. Data statistics are reported as mean and standard deviation. For the effects of the measurement errors on the result of the tests, see chapter 4.

Table 2.2 Definition of rudder's angles, all configurations - all measures are in deg.

	A		*B*		*C*	
Design δ_r	Mean	Std. Dev.	Mean	Std. Dev.	Mean	Std. Dev.
0.0	0.5	0.546	−0.4	0.258	−0.2	0.326
5.0	5.2	0.297	4.5	0.294	4.8	0.349
10.0	10.0	0.197	9.7	0.434	9.6	0.492
15.0	14.7	0.228	14.8	0.467	14.4	0.366
20.0	21.0	0.534	20.3	0.494	18.9	0.237
25.0	25.5	0.546	25.3	0.331	24.0	0.534
30.0	30.7	0.533	30.8	0.551	28.4	0.076

- №9 is the extended part of the stabilizer fixed on the lower part, №10 and 11 are the extended parts of the rudder. These are split in this way to have three different configurations with tails of $\mathcal{A}$R= 2.0: one full span, another 90% of span and the last 80% of span. These two parts are connected to the rudder by mean of a plug that allows the rotation, pins are inserted accordigly to have the above mentioned configurations.

In the figure 2.5 it is also shown the horizontal tail used for some configurations, it is part of the aircraft model model. Figure 2.7 shows the three vertical tail assemblies.

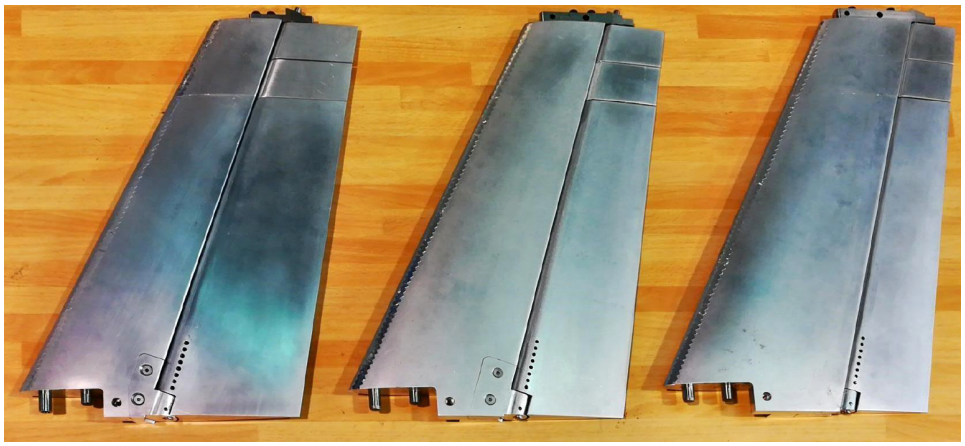

Figure 2.7 Tail assembly *A*, c_r/c = 0.45 (left), tail assembly *B*, c_r/c = 0.37 (center), tail assembly *C*, c_r/c = 0.30 (right).

Chapter 3

Approach to wind tunnel testing

3.1 Introduction

A wind tunnel is a tool used in experimental aerodynamic research to study the effects of air moving past solid objects: it consists of a tubular passage with the object under test mounted in the middle, air is made to move around the object by a powerful fan system or other means. The wind tunnel model is instrumented with suitable sensors to measure aerodynamic forces, pressure distribution, or other aerodynamic characteristics. The basic principle underlying its operation is the Galilean invariance, i.e. the laws of motion are the same in all inertial frames: having an aircraft at rest and the air moving toward it produces the same result as if the air is still and the aircraft is moving through it, in the same flow conditions.

3.1.1 History

The earliest wind tunnels were invented towards the end of the 19th century, in the early days of aeronautic research. The wind tunnel was envisioned as a means of reversing the usual paradigm: instead of the air standing still and an object moving at speed through it, the same effect would be obtained if the object stood still and the air moved at speed past it. Benjamin Robins (1707- 1751), an English military engineer and mathematician, invented a whirling arm apparatus to determine drag and did some of the first experiments in aviation theory. Sir George Cayley (1773-1857) also used a whirling arm to measure the drag and lift of various airfoils. However, at the end of the 19th century, the major fault of the whirling arm was apparent. This fault was due that the wing was forced to fly in its own wake. Francis Herbert Wenham (1824-1908), a Council Member of the Aeronautical Society of Great Britain, addressed these issues by inventing, designing, and operating the first enclosed wind tunnel in 1871. Konstantin Tsiolkovsky built an open-section wind tunnel with a centrifugal blower in 1897, and determined the drag coefficients of flat plates, cylinders, and spheres. In the early 1890s, a Danish inventor, Poul la Cour, applied wind tunnels in his process of developing technology of wind turbines.

Carl Rickard Nyberg used a wind tunnel when designing his Flugan from 1897 and onwards. In a classic set of experiments, the Englishman Osborne Reynolds (1842-1912), of the University of Manchester, demonstrated that the airflow pattern over a scale model would be the same for the full-scale vehicle if a certain flow parameter were the same in both cases. This factor, now known as the Reynolds number, is a basic parameter in the description of all fluid-flow situations. This comprises the central scientific justification for the use of models in wind tunnels to simulate real-life phenomena. The Wright brothers' use of a simple wind tunnel in 1901 to study the effects of airflow over various shapes while developing their Wright Flyer was in some ways revolutionary. In France, Gustave Eiffel (1832- 1923) built his first open-return wind tunnel in 1909, running about 4000 tests between 1909 and 1912 and contributing to set new standards for aeronautical research. Eiffel's contribution into improvement of the open-return wind tunnel by enclosing the test section in a chamber was followed by a number of wind tunnels later built (Eiffel was also the first to design a flared inlet with honeycomb flow straightener). Subsequent use of wind tunnels proliferated as the science of aerodynamics and discipline of aeronautical engineering were established and air travel and power were developed. The US Navy in 1916 built one of the largest wind tunnels in the world at that time at the Washington Navy Yard. Until the Second World War, the world's largest wind tunnel was built in 1932-1934 and located in a suburb of Paris, Chalais-Meudon, France. It was designed to test full size aircraft and had six large fans driven by high powered electric motors. The Chalais-Meudon wind tunnel was used by ONERA under the name S1Ch until 1976, contributing to the development of the Caravelle and Concorde airplanes. Actually, this wind tunnel is preserved as a national monument. During the Second World War large wind tunnels were built, and the development of wind tunnel science accompanied the development of the flying machines. In 1941 the US constructed one of the largest wind tunnels at that time at Wright Field in Dayton, Ohio. The wind tunnel used by German scientists at Peenemünde prior to and during WWII is an interesting example of the difficulties associated by extending the useful range of large wind tunnels. By the end of the Second World War, the US had built eight new wind tunnels, including the largest one in the world at Moffett Field near Sunnyvale, California, and a vertical wind tunnel at Wright Field. Later on, wind tunnel study came into its own: the effects of wind on man made structures or objects needed to be studied when buildings became tall enough to present large surfaces to the wind, and the resulting forces had to be resisted by the building's internal structure. Determining such forces was required before building codes could specify the required strength of such buildings and such tests continue to be used for large or unusual buildings. Still later, wind-tunnel testing was applied to automobiles, not so much to determine aerodynamic forces per se, but more to determine ways to reduce the power required to move the vehicle on roadways at a given speed.

3.2 DII wind tunnel

The experimental tests campaign has been performed in the main subsonic wind tunnel facility of the Department of Industrial Engineering (DII), figure 3.1. It is a subsonic, closed circuit tunnel, with a tempered rectangular cross section: the main characteristic are summarized in the Table 3.1, main components are described below, capital letters refer to the sections of Figure 3.2, then a list of instrumentation follows.

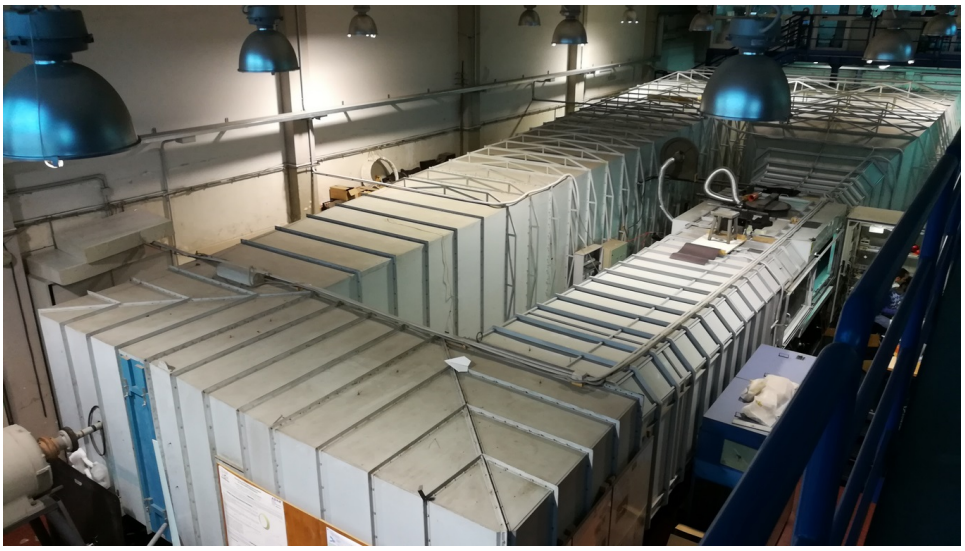

Figure 3.1 Main subsonic DII wind tunnel.

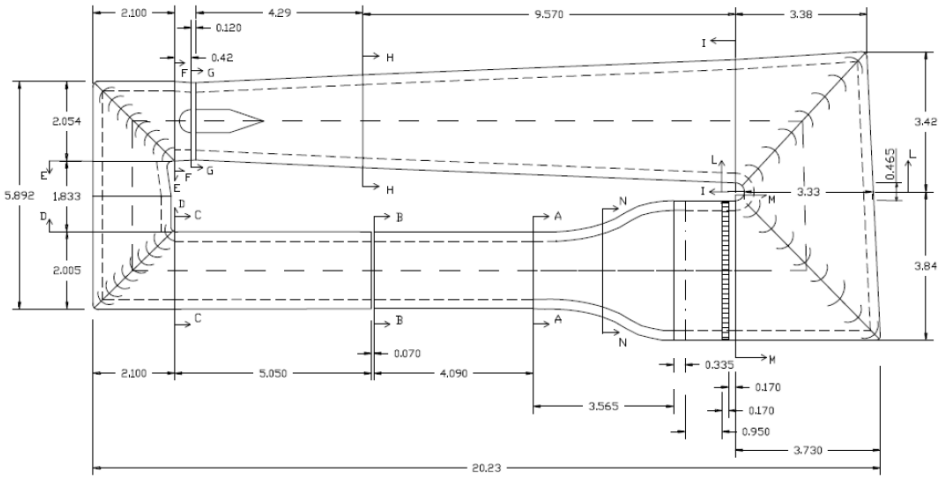

Figure 3.2 Main subsonic DII wind tunnel diagram.

Table 3.1 DII wind tunnel, main characteristics.

Test section dimensions	2.0 m × 1.4 m
Maximum avaiable wind speed	50 m/s
Turbolence level	0.10 %
Maximum power	150 kW

.a *Test section* - It is 4 m long, 2 m wide and 1.4 m high, with a rectangular cross-section of 2.68 m^2 with tempered corners. Sections from A to B.

.b *Diffuser* - There are three diffusers to slow down the airflow coming from the test chamber: the first one (B-C) has a length of about 5 m and an expansion angle of about 3 degrees, it links the last section of the test section to the first corner; the second diffuser (D-E) is placed between the first two corners and has a length of about 1.8 m; the last one (G-I) is the longest diffuser, about 12.3 m, it increases the tunnel section with an expansion angle of about 3 degrees and it is placed between the second and the third corner.

.c *Screen* - It is placed immediately before the first corner (section C), with the aim to protect the turning vanes against any possible object or scrap that could be lost by the model in the test section, it has a squared cells of about 13 mm per edge.

d. *Corners* - The first corner (C-D) is placed behind the first diffuser and has a constant section with turning vanes having a chord of about 450 mm and a maximum thickness of 14.1 %; the second one (E-F) is placed behind the fan and is equipped with tabs having a chord of about 490 mm and a maximum thickness of 13.3 %; the third corner (I-L) has diverters with a chord of 925 mm and a maximum thickness of 17.3 %; the fourth one (L-M) is equipped with tabs too having a length of 875 mm with a maximum thickness of 18.3 %. All corners, except the first one, are slightly divergent.

.e *Fan* - It is placed immediately ahead of the second corner (D-E) and made up of a six bladed propeller and a four bladed flow straightener ring placed upstream it, the ogive of the fan has a maximum diameter of 700 mm.

.f *Honeycomb flow straighteners* - They are elliptical section cells placed at the beginning of the stagnation chamber, section M.

.g *Mesh screen* - It has the fuction to reduce flow's turbolence axial component in the test section allowing a turbolence level of 0.10 %.

.h *Stagnation chamber* - It has a length of 0.035 m and it is placed ahead of the nozzle, section M.

.i *Nozzle* - It has a length of 3.56 m, with an inlet section of about 12.7 m^2 and an outlet section of 2.7 m^2 (a ratio of 4.83), sections from M to N.

Measurement instrumentation

- *Internal strain gage balance* - It has three channel used to measure the side-force, yawing and rolling moment, it is made from an Al-2024-T3 aluminium block. The balance has been subjected to a calibration procedure in order to perform a right exstimation of the aerodynamic force and moments, in addition the procedure is essential to estimate the balance center to transfer forces and moments to the desired reference point, e.g. the 25 %of the wing's main aerodynamic chord [7].

  The maximum error in average, found for the balance after the calibration, is about 0.1 %of the full scale maximum load of each measured force or moment. The actual balance readings have been deeply verified by applying the combination of predicted loads to be encountered during the tests. Corrections have been provided taking into account the combination of weight, pitching moment, rolling moment, and yawing moment, due to the particular layout of the test model, see Section 3.4.

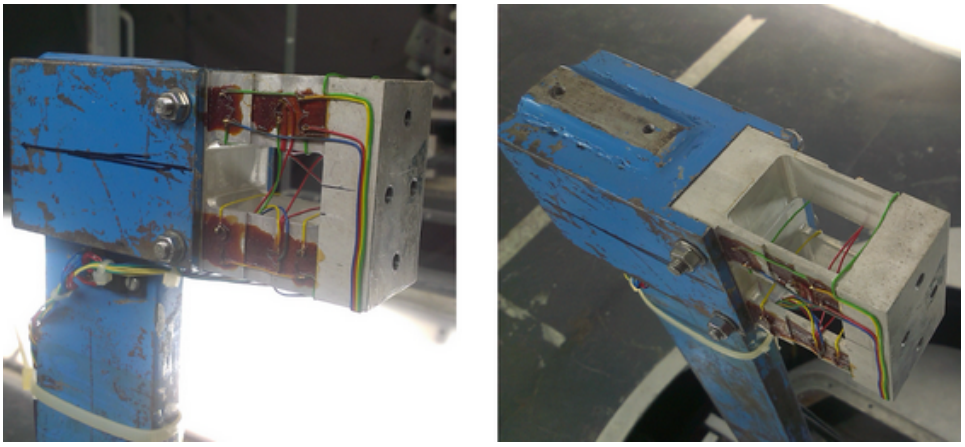

Figure 3.3 Lateral-directional internal strain gage balance.

- *Off-center load cell* - It is a Picotronik AAC model, used to directly measure the sideforce generated by the vertical tail. Made up from alluminium alloy, it has 15 kgf full scale, 2.0 mV/V ± 10 %nominal sensitivity and its dimensions are 130 × 30 × 22 mm. Calibration and installation are discussed in the Section 3.4.

- *Venturi* - DII wind tunnel is equipped with four static pressure probes, placed on both faces of the initial and final sections of the nozzle. A pressure transducer (2500 Pa full scale and 3 Pa accuracy) measures the static pressure

variation between these two sections and, through the continuity equation, gives the dynamic pressure at the exit of the nozzle. Several tests without the model in the test section and at different airspeeds have shown that the dynamic pressure at the end of the nozzle is 1.09 the measured dynamic pressure: since it is impossible to use a Pitot probe to measure the dyamic pressure in the test section in presence of the model (the test section should be long enough to guarantee that the measure is not affected by the pressure field produced by the model), the only avaiable measure is obtained by the Venturi, thus the 9 %increase is assumed to be valid with the model in the test section too.

- *Inclinometer* - It is the uni-axial tilt sensor CXLA01, produced by CrossBow (San Jose, CA, USA), and measures the component of the gravity's acceleration that lies in the plane of the instrumentation reference face. It has to be mounted on the sting of the wind tunnel balance.

- *Potentiometer* - It measures the sideslip angle with an accuracy of 0.1 degrees, once installed, the avaiable range for β is from -5 to 20 degrees. The sideslip angle has been defined positive when the airflow comes from the right.

- *Temperature probe* - It consist of a flush-mounted probe for the measure of the static temperature: the true test section speed is determined through the Bernoulli's incompressible equation, while the mass density is obtained through the equation of state. The temperature measurements are needed to keep under control the heating of the strain gage sensors too, which are effected by temperature change during a test (from 30 to 50 °C, according to enviromental temperature).

Control instrumentation

- It consist of a *kinematic mechanism* (handled by the operator) with a crank handle fixed at the end of a horizontal shaft acting as worm-screw, this shaft transmits the rotatory motion to the vertical axis of a small diameter gear wheel, this rotatory motion is then transmitted to a larger gear wheel through a steel chain reducing the angular speed of the model. A steel plate, which is at floor level, is fixed to the axis of the second gear wheel and allows the whole assembly sting-balance-model to rotate.

Instrumentation for acquisition and eleboration

- A 16 channels *SPARTAN* system (produced by Imc DataWorks, LLC) for the acquisition and conversion into 16 bit of output data coming from the measurement instrumentation. The default value of the acquisition and elaboration is 1000 samples in 1000 ms, by several preliminary tests this value has been finally changed to 200 samples at 100 Hz.

- A desktop *PC* with Windows XP, provided with an interface software for the A/D converter.
- The *WT6*, a software for the elaboration and visualization of the acquired data, developed at the DII laboratory.

3.3 Wind tunnel corrections

In wind tunnel testing there are some constraints due by the nature of the tunnel itself: while there is no difference in having the model at rest and the air moving around it, the distances of some or all the stream boundaries from the model are ususally less than the corresponding distances for actual operations, in addition the flow properties in the test section may not be the same in space and time. To include appropriate corrections, the following effects must be taken into account [8].

Horizontal buoyancy - It refers to a variation of the static pressure along the test section without the presence of the model in the test section. This variation produces a drag force analogous to the hydrostatic force on objects in a stationary fluid in a uniform gravitational field.

Solid blockage - It is linked to the model, which, occupying a certain volume in the test section, "chokes" the flow. It is the most influent effect since it produces a variation in oncoming dynamic pressure: this effect causes surface stresses larger than the corresponding free-air operations, the stress distribution is assumed to be unchanged.

Wake blockage - When a body is immersed in a moving fluid it produces a wake, whose size is function of the body shape and, in wind tunnel testing, of the ratio between the wake area and the tunnel area, this wake has a mean speed lower than the free stream. According to the law of continuity, the speed outside the wake in a closed tunnel must be higher than the free stream, by Bernoulli's principle this higher speed in the main stream has a lowered pressure: as the boundary layer on the model (which later becomes the wake) grows, the model is put in a pressure gradient, thus there is a speed increment on the model.

Streamline curvature - It refers to an alteration to the curvature of the streamlines of the flow about a body in a wind tunnel as compared to the corresponding curvature in an infinite stream. In a closed tunnel, the lift, pitching moment, hinge moments, and angle of attack are increased.

Normal downwash change - It refers to the component of induced flow in the lift direction at the test model and it is due to the finite distances to the boundaries. In a closed jet, the lift produced is too large and the drag too small at a given geometric angle of attack, corresponding to a smaller downwash.

Spanwise downwash distortion - It refers to an alteration to the local angle of attack along the span of a lifting wing: in a closed test section the angle of attack near the wingtips of a model with large span are increased, making the tip stall start at a lower geometric angle of attack. This effect becomes negligible if the model span is less than 0.8 the tunnel width.

Tail downwash change - It refers to an alteration to the normal downwash behind the wing, so that the static stability is unnaturally increased.

These effects have been assessed for the model in all configurations and inserted in the wind tunnel software to have in output both the corrected and uncorrected values. However, for the actual work focused on lateral-directional stability derivatives, differences between corrected and uncorrected results are not negligible only at high angles of sideslip, whereas the slope of the curves are unaffected by corrections.

3.4 Setup of the wind tunnel

A preliminary setup of the wind tunnel instrumentation, as well as of the test model, is needed before any operation. The measurement, control, and elaboration instrumentation must be checked. In particular, the wind tunnel balance readings must be verified. Then, the model can be mounted in the test section and the whole assembly can be verified in place. Finally, the effects of low Reynolds number can be measured and corrected.

The internal strain gage balance is a very delicate item, its verification consists in applying known loads in different position acquiring the balance readings: if the data are not consistent with the applied loads corrections must be provided by plotting regression lines that best fit curves on the chart of gathered data in all load conditions. It should be noticed that the center of gravity of the whole model is close to the balance center but not overlapped, so an offset is present between the lift and the balance center. Balance readings have been verified in several cases (figure 3.4) by varying the weight and the yawing moment: results provided that there is no affection on the yawing moment N by the eccentricity of the applied loads.

The off-center load cell measures forces on a single axis so the calibration procedure is very simple: its end with the acquisition cable has been fixed to a rigid constraint with the sensible side parallel to the ground, at the other end different known masses have been suspended. From the tension read, the tare constant has been calculated by mean of the linear relationship

$$\text{Force} = K_{cell} \cdot \text{Tension} \tag{3.1}$$

where K_{cell} has the dimension of kgf/V. The tare has then been verified by mountng the cell in the fuselage tail-cone and the vertical tail on the cell and applying a known

Figure 3.4 Verification of the internal strain gage balance.

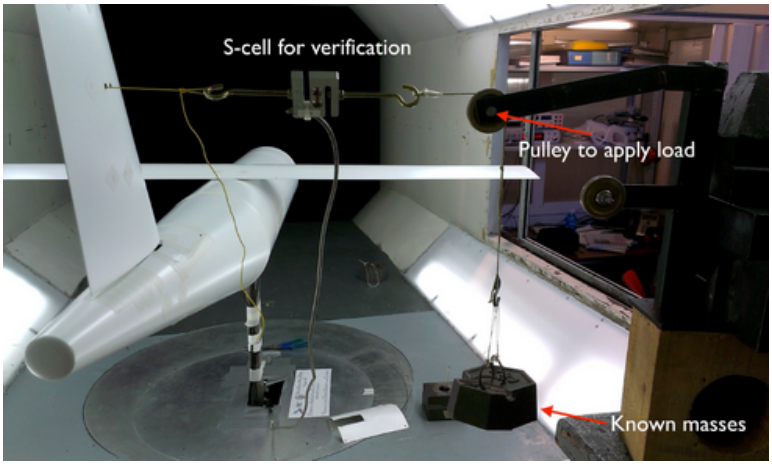

Figure 3.5 Test by application of a known mass.

mass in several position, see figure 3.5. With the term *scale effects* we refer to the differences that arise when the fluid dynamic dimensionless parameters, mainly the Reynolds number, are not the same in low-speed wind tunnel and flight conditons. Taking into account the definition of the Reynolds number

$$Re = \frac{\rho V c}{\mu} \tag{3.2}$$

where ρ is the air density, V the air speed, μ the air viscosity and c the wing mean aerodynamic chord, it is clear that full Reynolds number (for a large turboprop aircraft the characteristic wing chord is between 2.5 and 3.0 metres) are not achievable in a wind tunnel, in addition to the power requirements, unless the air temperature is decreased to reduce its viscosity and the total pressure is increased to arise the air density, as done in high speed wind tunnels. Since the Reyolds number of

low-speed wind tunnels cannot be the same of flight conditions, other artifices are needed to replicate the boundary layer of the full scale aircraft, otherwise laminar separations will affect the measurements. A simple and effective mean to comply with this need is the *trip strip*, which is an artificial roughness added to the model to fix the location of the transition from a laminar to turbulent boundary layer on the model [8].

A correct installation prevents the realization of laminar bubbles and their conseguences on the aerodynamic behaviour of the model, as shown in figure 3.7, laminar bubbles affect infact the slope of the curves expecially the vertical tail contribution. The aircraft model model had already been stripped accordingly to the study made by Ciliberti in [6], and the new tails has been stripped following the same procedure.

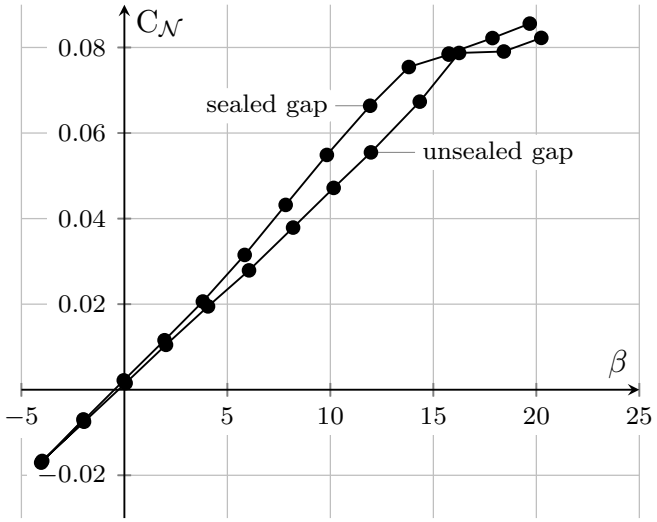

Figure 3.6 Effect of the rudder gap.

An additional effect took in consideration for the analysis of these tails is the gap that is present between the stabilizer and the rudder: its dimensions are negligible in a full scale tail and the flow is not affected by it, on the contrary, the actual gap has turned out to decrease the derivative $C_{\mathcal{N}_\beta}$ in the models, in particular reducing the vertical tail contribution by about 10% with respect to the value provided by the vertical tail without rudder of [6], as shown in the figure 3.6. The solution adopted was to seal this gap with tape.

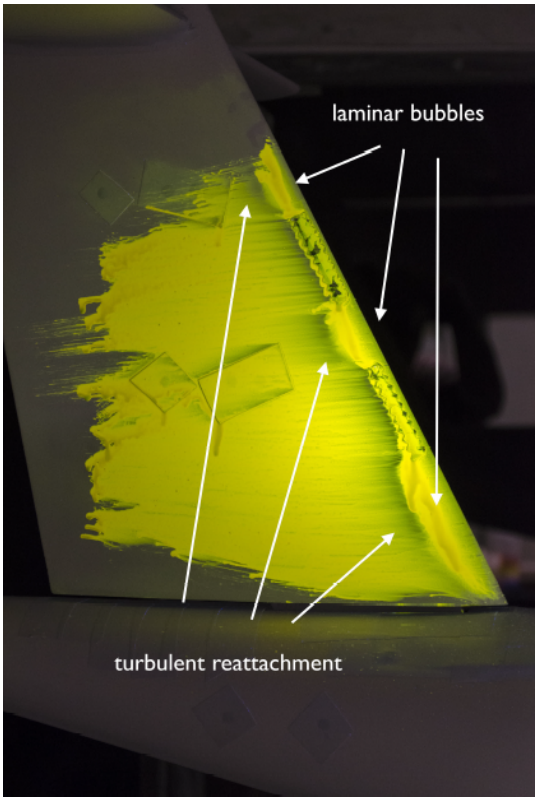

Figure 3.7 Strips' effect.

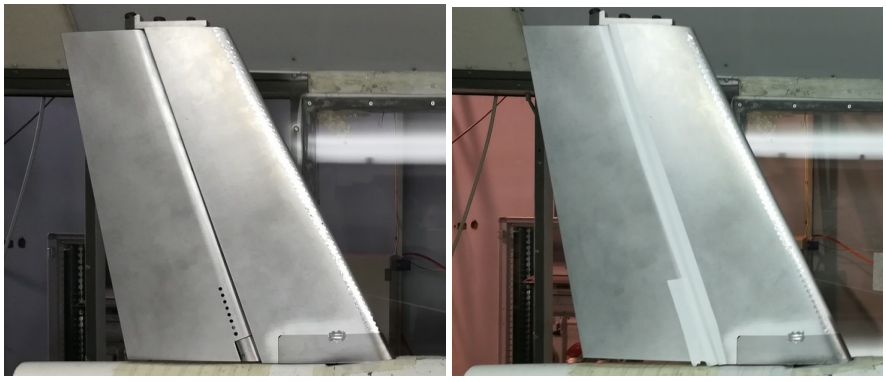

Figure 3.8 The tail assembly A involved in the investigation about the effects of the rudder gap. Re = 470 000, β = 0 deg.

Chapter 4

Results of the wind tunnel tests

4.1 Preamble

4.1.1 Reference system

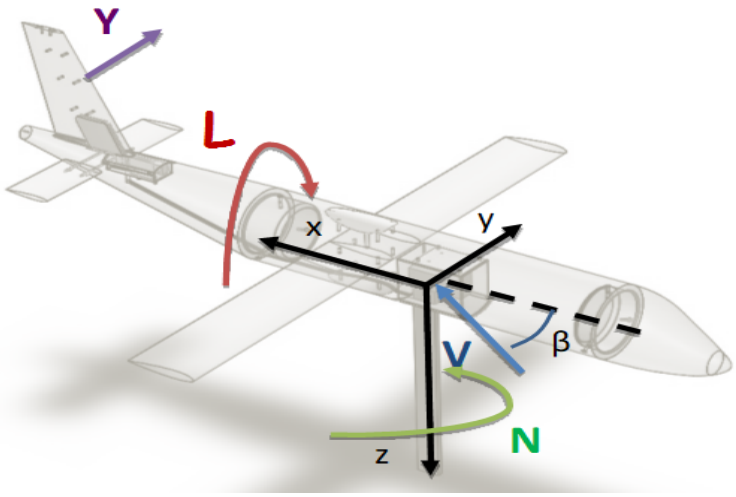

Figure 4.1 Reference system.

The reference system adopted, shown in figure 4.1, has the origin of the axes at the balance center, with the x axis parallel to the fuselage waterline and positive towards the fuselage stern, the y axis perpendicular to the symmetry plane and positive towards the left wing, and the z axis perpendicular to the other two and positive downward. The sideslip angle β is considered positive when the side wind is coming from the right wing. With this reference system, for a positive sideslip angle, the sideforce Y and the yawing moment $\mathcal{N}$ are both positive and the model is directionally stable, while a positive deflection of the rudder δ_r (trailing edge to the left of the model) produces a negative sideforce Y and yawing moment $\mathcal{N}$. In other words:

$C_{N_\beta} > 0$ is required for directional stability;
$C_{N_{\delta_r}} < 0$ is required for directional control.

Yawing moment and its derivative has been reduced to the mid wing aerodynamic center, whose location related to the balance center is shown in figure 4.2 (vertical tail aerodynamic centers are measured with respect to the balance center). The yawing moment coefficient derivative C_{N_β} and the vertical tail yawing moment coefficient derivative $C_{N_{\beta_v}}$, are approximated as the slope of the regression line

$$C_{x_\beta} = a + \frac{b}{\beta} \tag{4.1}$$

where C_{x_β} reprefents the generic derivative and the data points are limited within $-3° <= \beta <= 6°$. The Reynolds number based on wing mean aerodynamic chord for each test varies from 470000 down to 450000 because of the increasing flow temperature, which effects are included in the corrected results. Flow speed is held constant at 35 m/s and the angle of attack α is kept zero.

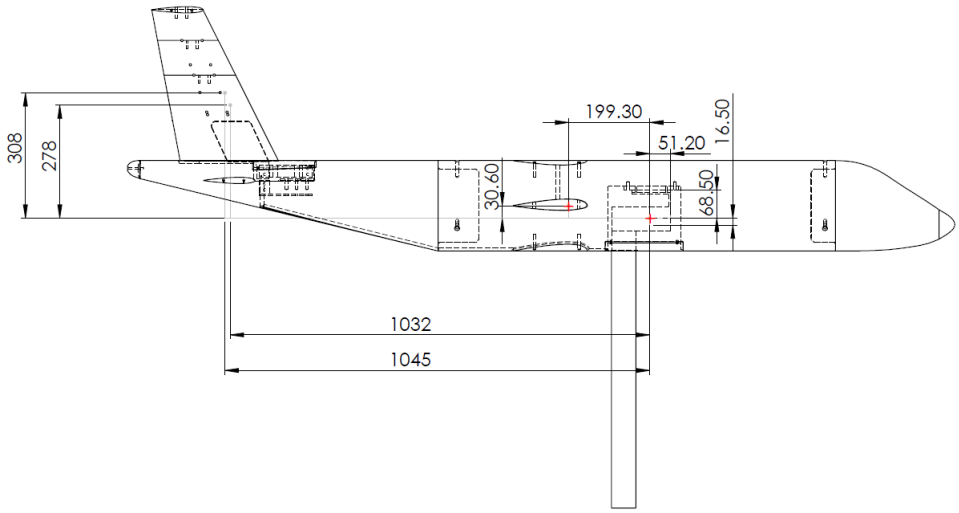

Figure 4.2 Relative position of moments reference points, units in mm.

4.1.2 Uncertainty of measurements

There are two types of uncertainties:

1. **Systematic** - These components produce the same result in repeated experiments, but different from the true value which remains unkwnown. Sources of systematic errors in this work are manufacturing and assembly ones: since the model should be symmetrical about its vertical plane, lateral-directional aerodynamic coefficients at no angle of sideslip should be zero, any deviation from this value has been considered as a systematic error. This type of error does not affect the slope of the curves but it is evaluated as a shift from the

original axes, the maximum deviation for the yawing moment coefficients has been measured from +0.0025 to +0.0100, due to the assembly and its mounting.

2. **Random** - These components produce different results in repeated experiments, assumed that all the controllable parameters are held as constant as possible. Sources of random errors in this work are: turbolence, enviroment temperature, instrumental accuracy, vibration during the tests and mounting tolerance among configurations. The true value of a quantity may be estimated by an accurate average of results' population, assuming that the calculated values are arranged in a Gaussian distribution with the relative standard deviation, as seen for the δ_r in section 2.2. All the effects on the derivatives are estimated accordingly and plotted as error bars.

Finally, the three basic principles in *design of experiments* [8] have been taken in consideration:
Replication, that refers to multiple repetitions of the basic experiments;
Randomization, that refers to the goal of producing replications of conditions for which the resulting experimental observations are stochastically indipendent;
Blocking, that refers to manipulations of the experimental conditions to isolate a particular effect. These three principles have already been discussed in Ciliberti's work [6].

4.1.3 Test procedure

The typical experimental test is structured as follow:

1. *Setup of the configuration* - The model is set by the operator in the selected configuration. A list of all of them has been made in order to switch among configurations in a short time.

2. *Data acquisition* - The model is set at zero sideslip condition, the *WT*6 program is executed and the zero for all the measurement instrumentation is set then the tunnel is started and led to the operative conditions (35 m/s). After having waited a time interval of 1 minute and a half, so that the flow has stabilized in a stationary condition, the first value is acquired, then the model is turned at first to the negative sideslip angles, subsequently the operator brings it back to the initial attitude and the sampling continues till the sideslip angle of about +18 degrees, with a sampling step of about 2 degrees.

3. *Data elaboration and storage* - The aerodynamic forces and moments coefficients are calculated by the acquired measurement of forces and dynamc pressure. All the data are saved in specific a folder with an appropriate label.

The nomenclature of the labels used to identify the configurations is as follows, aircraft compnents IDs are separated by underscores _

Body is indicated by two letters,

BH	body high
BL	body low

Wing (if present) is indicated by two letters,

WH	wing high
WL	wing low

Vertical tail (if present) is indicated by a first letter that indicates the tail assembly, a letter and two digits for the aspect ratio and a letter and two or three digits for the span,

A	tail assembly A
B	tail assembly B
C	tail assembly C
V15	$AR = 1.5$
V20	$AR = 2.0$
E100	100% of the span
E90	90% of the span
E80	80% of the span

Rudder deflection is indicated by a letter and one or two digits,

D0	$\delta_r = 0$ deg
D05	$\delta_r = 5$ deg
D10	$\delta_r = 10$ deg
D15	$\delta_r = 15$ deg
D20	$\delta_r = 20$ deg
D25	$\delta_r = 25$ deg
D30	$\delta_r = 30$ deg

Horizontal tail (if present) is indicated by a letter and a digit,

H1	body-munted horizontal tail
H5	T-tail configuration

Example: `BH_WH_V15_H1_A_E100` indicates the configuration with high fuselage, high wing, body-mouted horizontal tail and tail assembly *A* with aspect ratio $AR = 1.5$ and full span. For each configuration a set of seven tests has been performed to collect the data from each rudder deflection possible (from `D0` to `D30`). A total of 42 configurations involving the vertical tail have been assembled and tested for each rudder deflection (294 runs), while 6 configurations without the vertical tail have been performed for the comparison between the measures of the internal balance and the off-center load cell (for a total of 300 runs).

4.2 Directional control results

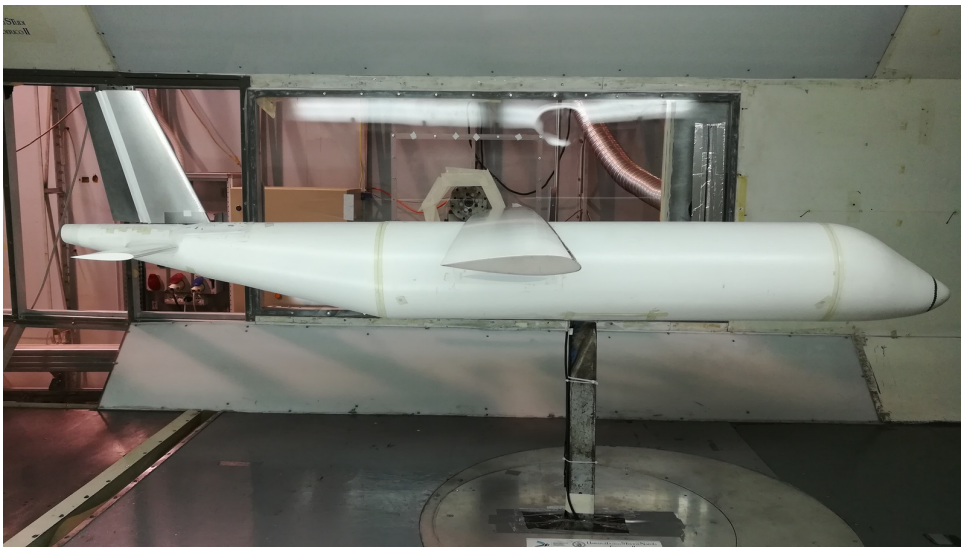

Figure 4.3 Assembly *B* with an aspect ratio of 1.5, body tail cone high, wing high, body-mounted horizontal tail. $Re = 470000$, $\alpha = 0°$

The first result that should be analyzed is the effect of a rudder deflection on the yawing moment coefficient $C_{\mathcal{N}}$. It has to be remarked that this coefficient in a preliminary design phase can be divided into two contributions:

$$C_{\mathcal{N}} = C_{\mathcal{N}_{\delta_r}} \delta_r + C_{\mathcal{N}_\beta} \beta \tag{4.2}$$

The configuration involved in this section refers to a general turboprop aircraft with high wing, body-mounted horizontal tail and a vertical tail with a typical $c_r/c = 0.37$ and $\mathcal{AR} = 1.5$, see figure 4.3.

At no sideslip, the airplane is in symmetric flight conditions, the introduction of a rudder deflection generates a local angle of sideslip close to the vertical tail and the flow's simmetry is lost. The main effect is a generation of a sideforce Y along the negative y axis (a positive δ_r generates a negative local sideforce), and a negative yawing moment $\mathcal{N}$. In terms of coefficients, the $C_{\mathcal{N}}$ and $C_{\mathcal{N}_v}$ versus β curves are reported in Figures 4.4 and 4.5, as stated previously rudder's deflection shifts the curves to the lower right part of the chart. A second effect is that for a positive δ_r deflection the vertical tail is able to keep the aircraft in directional equilibrium (absence of a resulting lateral force) at increasing sideslip angle β: this increase is almost constant till a $\delta_r = 20\,°$, then, the appearing of non-linear effects, decreasing the rudder effectiveness, reduces this influence up to cancel it, in fact the successive curves tend to overlap.

For a given β the value of the equilibrium $\delta_{r_{\text{eq}}}$ can be calculated from the eq. 4.2 by imposing that $C_{\mathcal{N}} = 0$: this aspect is strictly connected to the cross wind condition

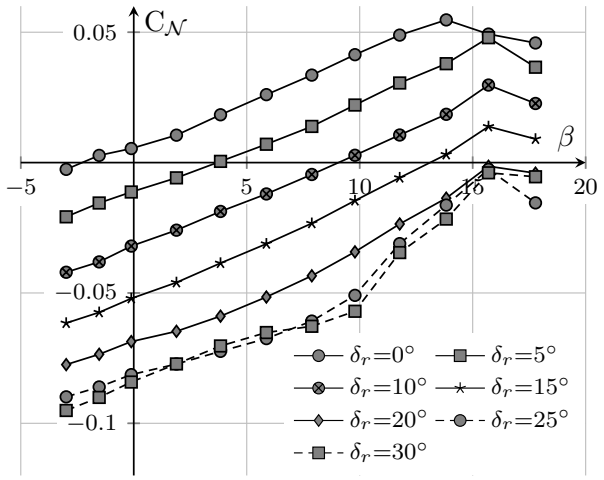

Figure 4.4 Yawing moment coefficient, $C_{\mathcal{N}}$ vs sideslip angle, β - Internal straing gage balance readings.

during take-offs and landings for the sizing of the vertical tail. Figure 4.6 shows the values of $\delta_{r_{\text{eq}}}$ given by the equation for the configuration `BH_WH_H1_B_V15`, however this calculation is just an indication about the trend of the curve and the actual values do not have to be taken in consideration.

The $C_{\mathcal{N}_v}$ contribution of the vertical tail to the yawing moment coefficient was measured by the off-center load cell and the $C_{\mathcal{N}_{v_\beta}}$ derivative has been calculated with eq. 4.1. Without a device to directly measure the vertical tail aerodynamic force *in situ*, this coefficient can be evaluated as difference between the $C_{\mathcal{N}}$ of the whole configuration and the $C_{\mathcal{N}}$ of the same configuration without the vertical tail.

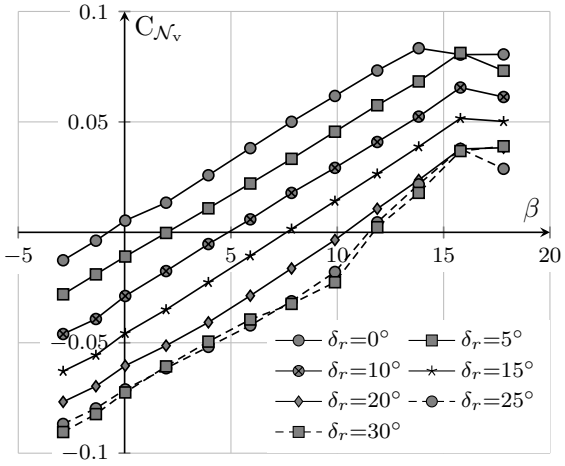

Figure 4.5 Yawing moment coefficient of the vertical tail, $C_{\mathcal{N}_v}$ vs sideslip angle, β - Off-center load cell readings.

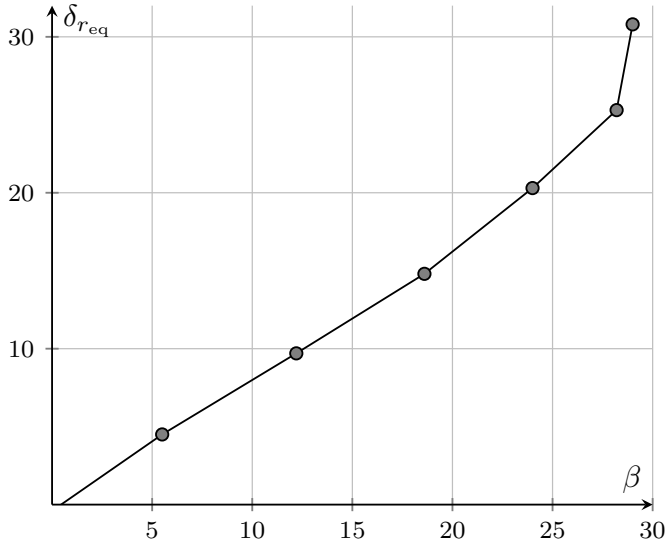

Figure 4.6 Equilibrium rudder deflection, $\delta_{r_{\text{eq}}}$ vs the sideslip angle, β.

Figure 4.7 shows a comparison of the two approaches: the curves intersect near the equilibrium angle with different slopes, with the tri-axial balance having the higher slope. This increase of the slope is almost constant and 15% higher than the slope of the vertical tail load cell. It is due to a mutual aerodynamical interference that arises among all the aircraft components and changes the actual values of the derivatives, see Section 4.5 for a more detailed discussion.

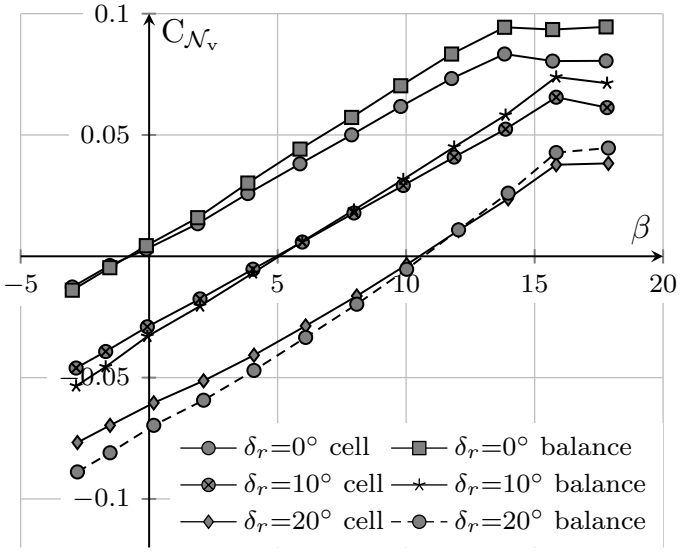

Figure 4.7 Yawing moment coefficient of the vertical tail, $C_{\mathcal{N}_v}$ vs sideslip angle, β - cell vs balance readings.

The vertical tail rudder effectiveness τ_v is evaluated as the ratio of the directional control derivative to the directional stability derivative at zero sideslip angle

$$\tau_v = \left| \frac{C_{N_{v_{\delta r}}}}{C_{N_{v_\beta}}} \right|_{\beta=0^\circ} \tag{4.3}$$

Figures 4.8 and 4.9 show the typical trend of these derivatives for the chosen configuration: for low δ_r they have an almost constant behaviour, then around δ_r= 20° there is a reduction in absolute values of both terms. It can be noticed that the shift between the values misured by the cell and the balance is constant for all the range of rudder deflections.

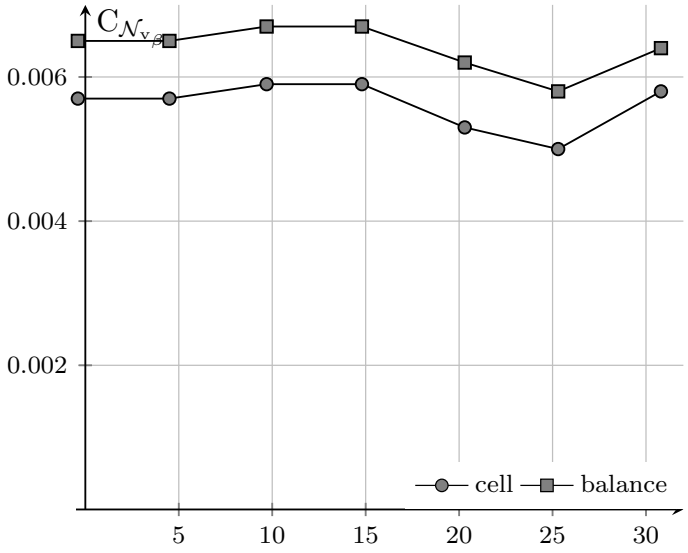

Figure 4.8 Yawing moment coefficient derivative of the vertical tail, $C_{N_{v_\beta}}$ vs rudder deflection, δ_r - `BH_WH_H1_B_V15`.

In this case, the evaluation of the yawing moment coefficient by difference of the balance readings with and without the vertical tail has led to an overestimation of the rudder control power $C_{N_{v_{\delta r}}}$. Although equilibrium, stability, and control involve the whole aircraft, an incorrect evaluation of the vertical tail contribution may led to sizing errors. For instance, the aircraft could not comply to minimum control speed requirement (critical for design, involving take-off length), or keep equilibrium for a lateral wind gust.

Figure 4.10, finally, shows τ_v's curves derived from 4.3, that have the same trend of their components. The amplifications on the slope $C_{N_{v_\beta}}$ given by the balance readings is specular to those on the control power derivatives $C_{N_{v_{\delta r}}}$, thus the two effectiveness curves are almost overlapped, the slight difference that occur increases with the rudder deflection but does not exceed the 2.3%.

The error bars plotted are simmetrical to the data point acquired: the horizontal bars refer to the standard deviation of the rudder's angles of deflection, reported in

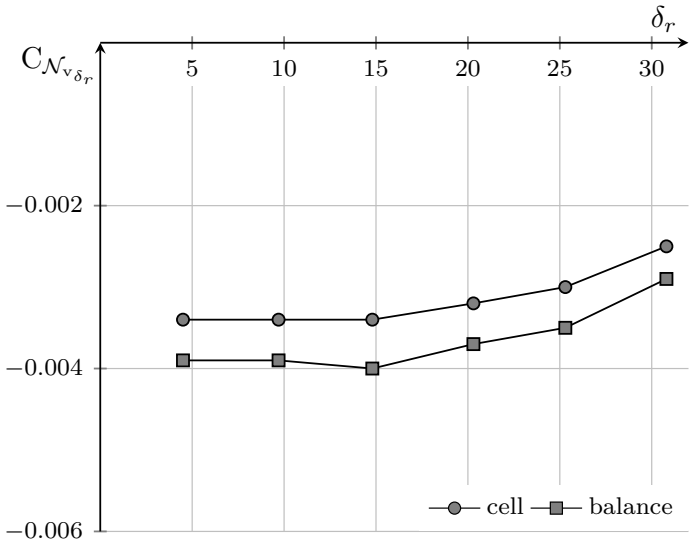

Figure 4.9 Control power, $C_{\mathcal{N}_{v_{\delta_r}}}$ vs rudder deflection, δ_r - `BH_WH_H1_B_V15`.

table 2.2 at page 24; the vertical bars are calculated with the equation:

$$\sigma_\tau = \bar{\tau}\sqrt{\left(\frac{\sigma_{C_{\mathcal{N}_\beta}}}{\overline{C_{\mathcal{N}_\beta}}}\right)^2 + \left(\frac{\sigma_{C_{\mathcal{N}_{\delta_r}}}}{\overline{C_{\mathcal{N}_{\delta_r}}}}\right)^2} \tag{4.4}$$

representing the errors propagation, where the overbarred derivatives are estimates of the true derivatives for a given $\bar{\delta_r}$ (values assumed for δ_r of Table 2.2), the maximum value of the relative error (σ_τ/τ) is about 2.1%.

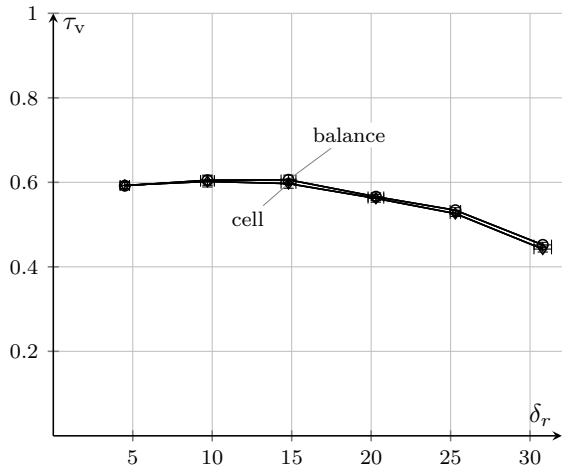

Figure 4.10 Vertical tail effectiveness, τ_v vs rudder deflection, δ_r - evaluated from the curves of Figure 4.7.

4.3 Vertical tail effectiveness

The effectiveness τ_v of a vertical tail is the key characteristic for an accurate sizing. This coefficient is function of different factors:

$$\tau_v = f\,(c_r/c, AR, \delta_r, \eta_v) \tag{4.5}$$

where c_r/c (or c_r/c_v) is the rudder's chord fraction, behind the hinge line as shown in Figure 2.4, respect to the vertical tail's chord (the percentage is constant on the full span), AR is the vertical tail aspect ratio, δ_r is the rudder deflection angle and η_v is the dynamic pressure ratio ρ_v/ρ_∞ (usually < 1).

Through the experimental test campaign we were able to evaluate the effectiveness for several configuration, including partial aircraft like the isolated vertical tail (V - Figure 4.11). For the isolated vertical tail, the aerodynamic interference of the support is taken into account by subtracting it from the acquired data and the results have been scaled to the aircraft model vertical tail moment arm.

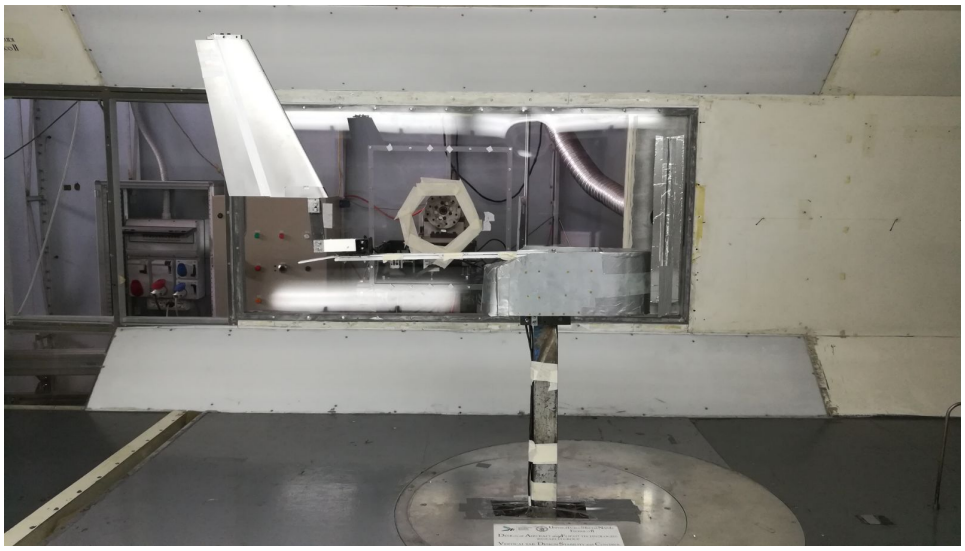

Figure 4.11 Vertical tail isolated configuration, tail assembly *B* with AR = 2.0 - V

For these configurations it is interesting to investigate the influence of those parameters on the effectiveness to get some indications on the vertical tail's sizing.

The first effect analyzed is the change in rudder chord's fraction of the vertical tail, c_r/c. Each tail assembly was tested for both aspect ratios, Figure 4.12 shows the three different τ_v for AR= 2.0.

It can be seen that an increasing on the chord's length corresponds to an increasing of the vertical tail's contribution to the effectiveness: all the assemblies have the same planform area so more rudder chord fraction means that more area of the tail acts as control surface and the effectiveness holds higher values for a given δ_r.

In conjunction to a comparison on the vertical tail's effectiveness Figure 4.13 shows a comparison in terms of equilibrium's angles: a bigger rudder achieves directional equilibrium at higher sideslip angles.

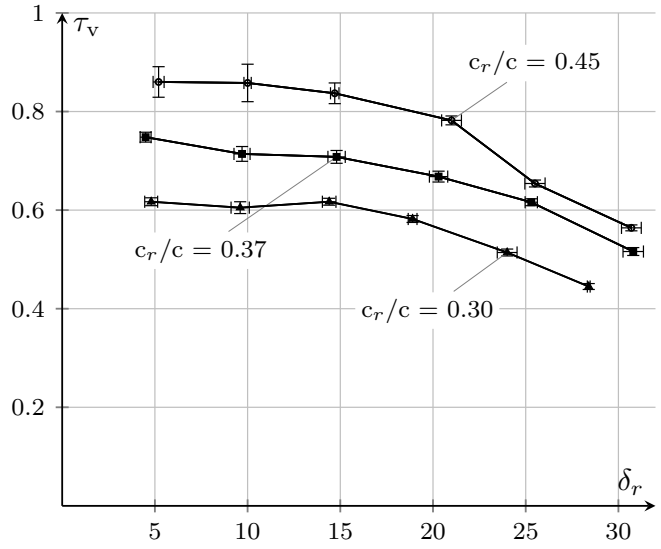

Figure 4.12 Effect of the rudder chord ratio on vertical tail effectiveness.

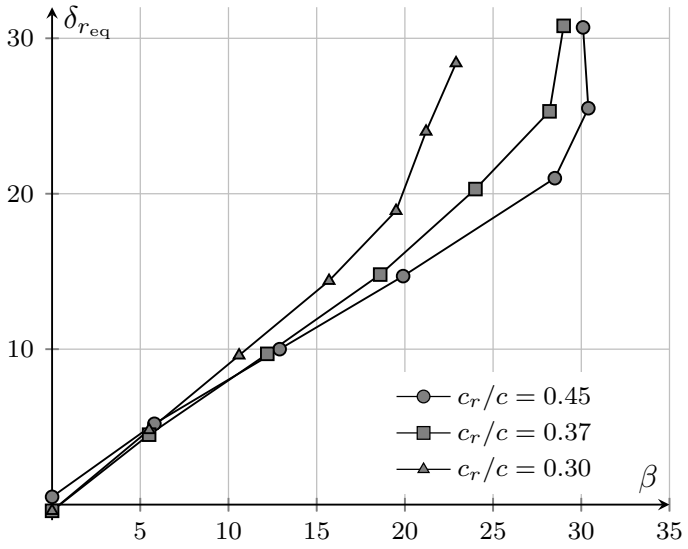

Figure 4.13 Effect of the rudder chord ratio on the equilibrium angle, $\delta_{r_{\mathrm{eq}}}$.

Another factor of influence is the change in *Aspect Ratio* AR. Figures 4.14 and 4.15 show a comparison in terms of vertical tail's effectiveness τ_v and equilibrium δ_r respectively for the tail assembly *B* isolated and both aspect ratios. As regards the effectiveness the tails have the same behaviour, however the tail with the higher ARprovides a lower value of the effectiveness for a given rudder deflection: till a δ_r = 20° this difference is of about 3-5%, then it begins to increase during the effectiveness' fall due to tri-dimensional effects that occurs for high values of δ_r which have a greater effect on this tail. In addition the tail with the shorter ARachieves higher sideslip angles at full rudder deflection, being more effective.

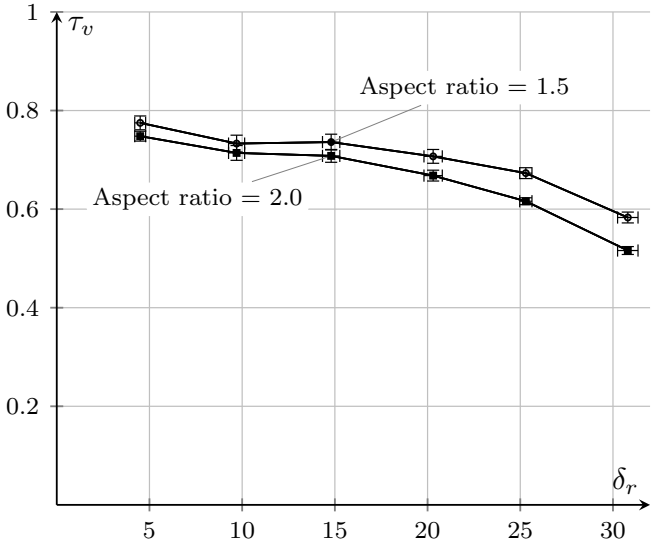

Figure 4.14 Effect of the aspect ratio on the rudder effectiveness, τ_v.

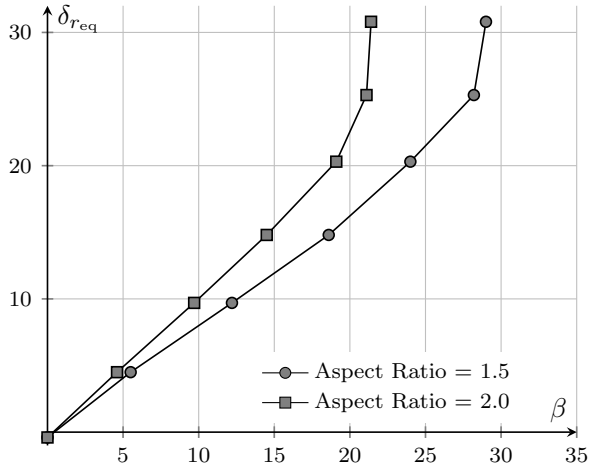

Figure 4.15 Effect of the vertical tail aspect ratio on the equilibrium angle, $\delta_{r_{eq}}$.

(a) 100% of span **(b)** 90% of span **(c)** 80% of span

Figure 4.16 Different span lengths, tail assembly B.

A third aspect is linked to the span of the rudder that can be modified for the tail models with aspect ratio equal to 2.0. Figure 4.16 shows a $\delta_r = 30°$ deflection for each configuration. For the configurations with reduced span, the rudder parts held fixed act as a chordwise extension of the stabilizer. In Figure 4.17 a comparison in terms of rudder's effectiveness is shown for the assembly B, the configuration involved in this investigation is a partial configuration without the horizontal tail (body high, wing high, vertical tail): a reduction on the span length results in a reduction of the vertical tail's effectiveness, this effect is more remarkable for the shorter span but it does not exceed the 10% of the value for the full span. A reduction on the span length results in a reduction of the the equilibrium δ_r too, see Figure 4.18.

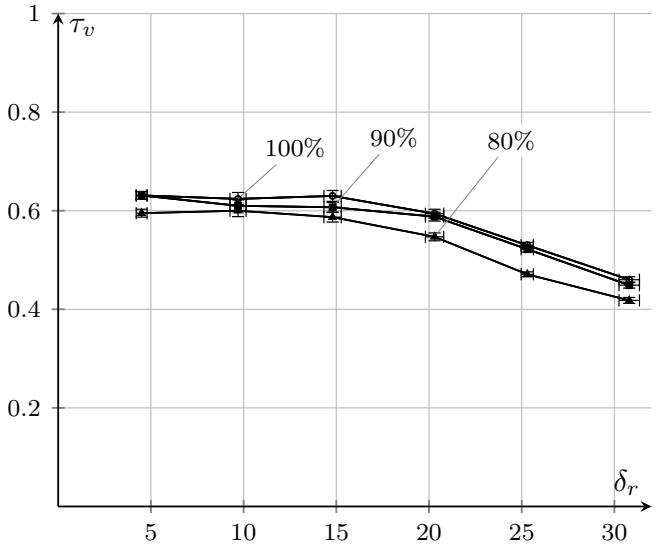

Figure 4.17 Effect of the rudder span ratio on the rudder effectiveness, τ_v.

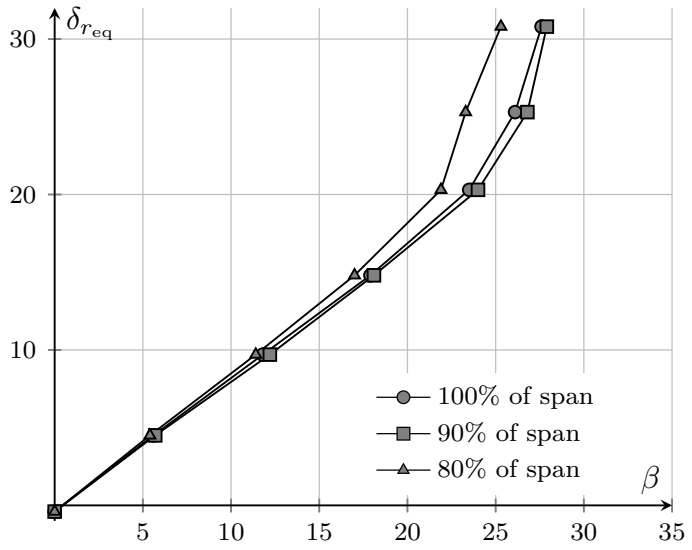

Figure 4.18 Comparison of $\delta_{r_{\text{eq}}}$ for different span percentage.

4.3.1 Comparison with semi-empirical methods

In a preliminary design phase the rudder effectiveness is usually evaluated by mean of semi-empirical methods like *McCormick* [9], *Roskam* [10] or *Torenbeek* [11]. These methods provide different results and have not a great accuracy, especially for high values of rudder's deflection (δ_r > 20°) [12] [3].

Here follows a comparison between the semi-empirical methods and the data acquired from the wind tunnel tests: Figure 4.19 in terms of ÆRand Figure 4.20 in terms of c_r/c.

As it can be seen from the graphs in almost all the range of rudder deflections the semi-empirical methods underestimate the effectiveness, in particular there is no difference between the two aspect ratios (the curves are completely overlapped, while the two experimental curves from 4.14 are clearly distinguishable) while the increase that was estimated for the change in rudder's chord of Figure 4.12 results to be smaller and always constant except for the *Roskam* that for small rudder deflections (δ_r = 10-20°) gives an estimation more similar to reality, at least for the smaller rudder's fractions of chord.

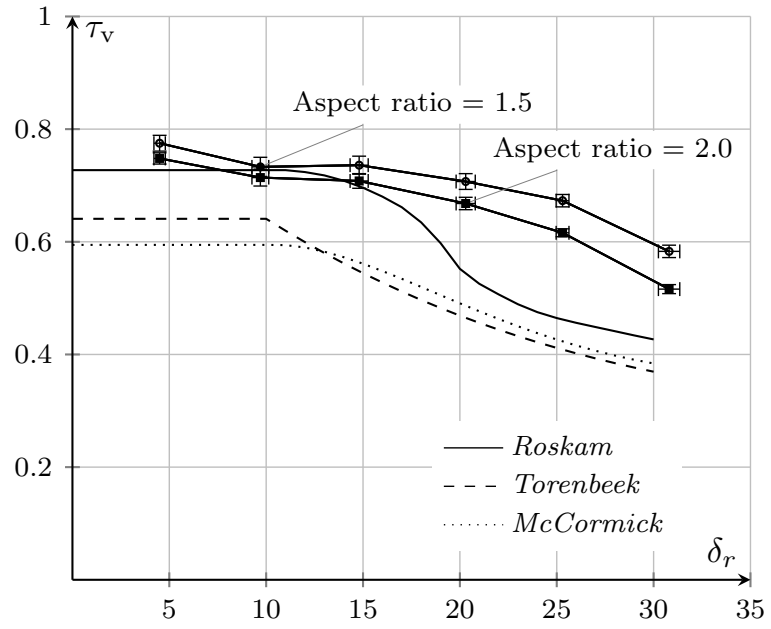

Figure 4.19 Comparison of τ_v for different aspect ratios - semi-empirical methods vs wind tunnel tests result.

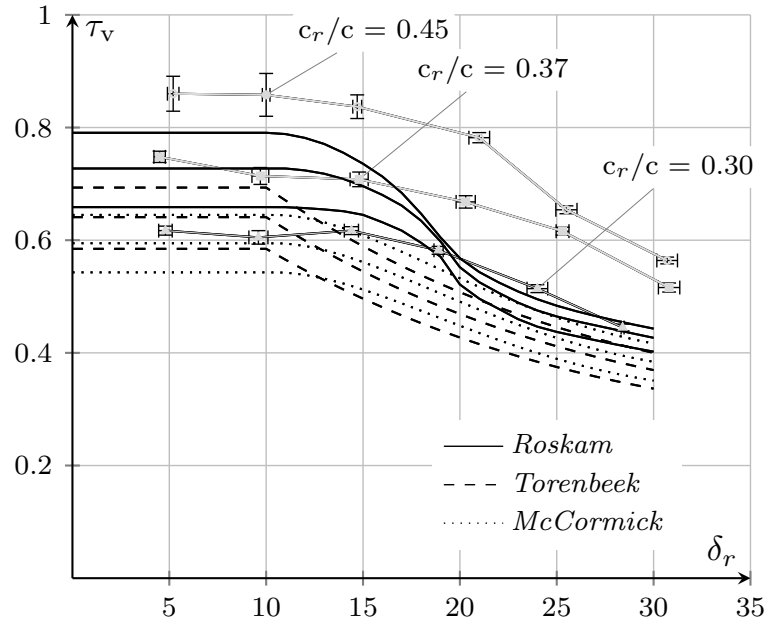

Figure 4.20 Comparison of τ_v for different rudder's chord fraction - semi-empirical methods vs wind tunnel tests result.

4.4 A method for the calculation of the rudder effectiveness

A method for the calculation of the rudder effectiveness can be suggested thanks to the K coefficients evaluated in this section

$$\tau_{\mathrm{v}} = \tau_{\mathrm{v_{ref}}}(\delta_r) K_{\mathrm{chord}} K_{\mathrm{AR}} K_{\mathrm{span}} \tag{4.6}$$

where the first parameter is the effectiveness of the tail assembly B with $\mathcal{R} = 2.0$ and full span, which is the reference parameter from which each coefficient K is calculated and is dependent only by the rudder deflection δ_r, it is reported in Figure 4.21. Each coefficient takes into account one of the three different geometrical aspects described (c_r/c, $\mathcal{R}$, η), keeping constant the other two, and is dependent by the rudder deflection too.

For each set of data trend lines are plotted in order to have an expression for the K coefficients in function of δ_r. The curve relative to the reference effectiveness is equal to the unit value for construction, the other curves reflect the same behaviour of the effectiveness from which they are calculated. The K parameters are amplification (or reduction) of separate effects. The value of $\tau_{\mathrm{v_{ref}}}$ is given by the following polinomial approximation

$$\tau_{\mathrm{v_{ref}}}(\delta_r) = -0.000516\delta_r^2 + 0.011624\delta_r + 0.648369 \tag{4.7}$$

The vertical error bars plotted are evaluated with the 4.4 equation (K is the ratio between two effectiveness).

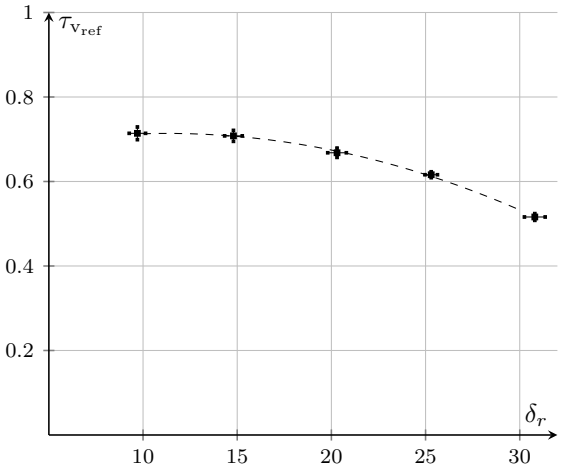

Figure 4.21 Effectiveness of reference from the equation 4.6.

The first coefficient, K_{chord}, takes into account the effect of the chord ratio, c_r/c, Figure 4.22.

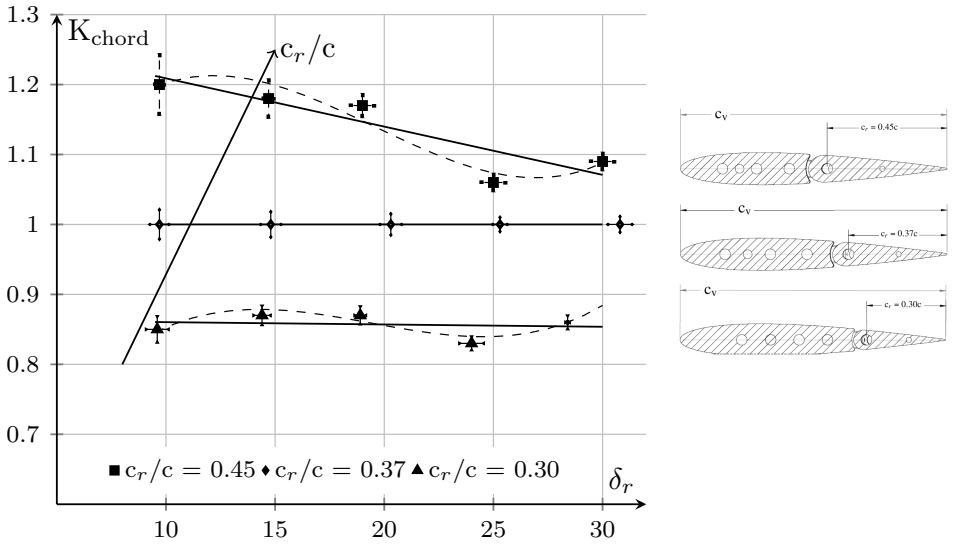

Figure 4.22 K_{chord} estimation vs rudder deflections.

The second coefficient, K_{AR}, takes into account the effect of the aspect ratio, *AR*, Figure 4.23.

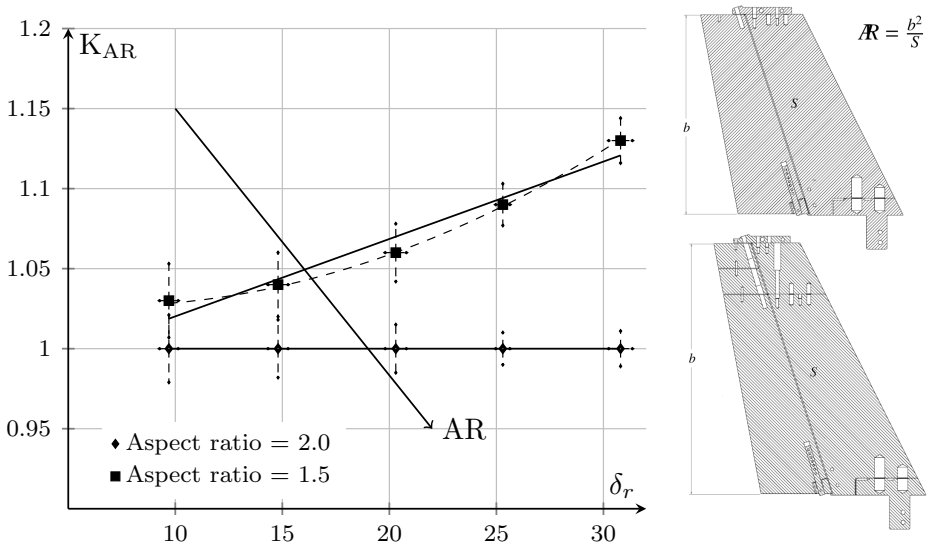

Figure 4.23 K_{AR} estimation vs rudder deflections.

The third coefficient, K_{span}, takes into account the effect of the rudder extension along the span, η, Figure 4.24.

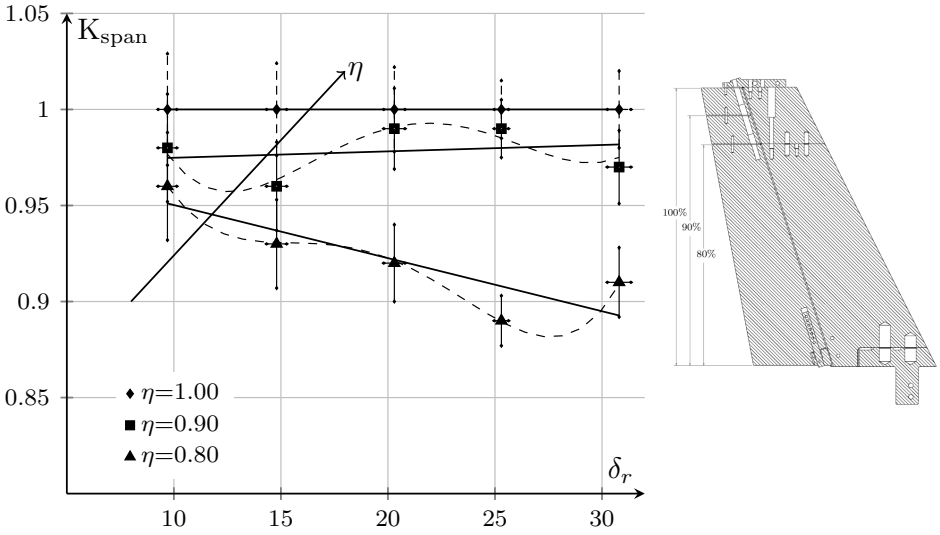

Figure 4.24 K_{span} estimation vs rudder deflections.

A first check to the method can be done by calculating the effectiveness of each point used to build the method itself. For istance take into consideration the K_{AR} coefficient (Figure 4.23): two curves were parameterized for the $\mathcal{R} = 1.5$ experimental data points, one linear and the second parabolic.

$$K_{\mathrm{AR}}|_{1.5} = 0.004835\delta_r + 0.971828 \tag{4.8}$$

$$K_{\mathrm{AR}}|_{1.5} = 0.000176\delta_r^2 - 0.002281\delta_r + 1.033837 \tag{4.9}$$

By keeping constant the fraction of the rudder chord (K_{chord}=1.00) and the span (K_{span}=1.00), the effectiveness of a tail with aspect ratio = 1.5 is calculated by mean of

$$\tau_{\mathrm{AR}_{1.5}} = K_{\mathrm{AR}}|_{1.5}\tau_{\mathrm{ref}} \tag{4.10}$$

once using the 4.8 and again using the 4.9. The results were compared to the measured values and reported in Table 4.1.

Both approaches show a good agreement with the experimental results, the linear approximation returns values with a maximum error of 1.15%, thus the 4.8 is a good choice.

A similar procedure was used for the other two coefficients. Results are reported from Table 4.2 to 4.5: linear trends were compared to polinomial expressions and in almost every case the error is less than 2-3% for the linear curves.

Here follow the linear equations used to calculate each coefficient.

$$K_{\mathrm{chord}}|_{0.45} = -0.006903\delta_r + 1.277872 \tag{4.11}$$

Table 4.1 Comparison between the experimental measurement and the results of the 4.10.

$\delta_{r_{\text{ref}}}$ (deg)	τ_{ref}	experimental measurement	$\tau_{\text{AR}_{1.5}}$ linear	ϵ	$\tau_{\text{AR}_{1.5}}$ parabolic	ϵ
10	0.713	0.733	0.727	-0.77%	0.733	+0.06%
15	0.708	0.736	0.739	+0.44%	0.735	-0.04%
20	0.668	0.707	0.714	+1.01%	0.707	+0.08%
25	0.616	0.673	0.674	+0.15%	0.670	-0.38%
30	0.516	0.583	0.577	-1.15%	0.580	-0.51%

Table 4.2 Comparison between the experimental measurement and the results of the 4.6 in terms of K_{chord} for $c_r/c = 0.45$.

$\delta_{r_{\text{ref}}}$ (deg)	τ_{ref}	experimental measurement	$\tau_{\text{chord}}\|_{0.45}$ linear	ϵ	$\tau_{\text{chord}}\|_{0.45}$ parabolic	ϵ
10	0.713	0.858	0.862	+0.47%	0.857	-0.08%
15	0.708	0.837	0.831	-0.77%	0.848	+1.31%
20	0.668	0.782	0.761	-2.70%	0.768	-1.86%
25	0.616	0.654	0.680	4.01%	0.662	+1.22%
30	0.516	0.564	0.553	-1.89%	0.562	-0.33%

$$K_{\text{chord}}|_{0.30} = -0.000325\delta_r + 0.863619 \tag{4.12}$$

$$K_{\text{span}}|_{0.90} = 0.000334\delta_r + 0.971515 \tag{4.13}$$

$$K_{\text{span}}|_{0.80} = -0.002765\delta_r + 0.977694 \tag{4.14}$$

Once all the trend are defined, a linear interpolation between curves can be done to evaluate the effectiveness for different values of c_r/c, *A*Rand η, here follow the equations.

$$K_{\text{chord}}|_{new} = K_{\text{chord}}|_{0.30}(\delta_r) + \frac{K_{\text{chord}}|_{0.45}(\delta_r) - K_{\text{chord}}|_{0.30}(\delta_r)}{0.15}(c_r/c|_{new} - 0.30) \tag{4.15}$$

$$K_{\text{AR}}|_{new} = 1 + \frac{K_{\text{AR}}|_{1.5}(\delta_r) - 1}{0.5}(2.0 - \text{AR}|_{new}) \tag{4.16}$$

$$K_{\text{span}}|_{new} = K_{\text{span}}|_{0.80}(\delta_r) + \frac{1 - K_{\text{span}}|_{0.80}(\delta_r)}{0.20}(\eta|_{new} - 0.80) \tag{4.17}$$

Table 4.3 Comparison between the experimental measurement and the results of the 4.6 in terms of K_{chord} for $c_r/c = 0.30$.

$\delta_{r_{ref}}$ (deg)	τ_{ref}	experimental measurement	$\tau_{chord}\|_{0.30}$ linear	ϵ	$\tau_{chord}\|_{0.30}$ parabolic	ϵ
10	0.713	0.605	0.616	+1.69%	0.608	+0.45%
15	0.708	0.617	0.611	-0.95%	0.621	+0.73%
20	0.668	0.582	0.577	-0.97%	0.576	-1.14%
25	0.616	0.514	0.532	+3.63%	0.518	+0.77%
30	0.516	0.445	0.446	+0.25%	0.457	+2.66%

Table 4.4 Comparison between the experimental measurement and the results of the 4.6 in terms of K_{span} for $\eta = 0.9$.

$\delta_{r_{ref}}$ (deg)	τ_{ref}	experimental measurement	$\tau_{span}\|_{0.90}$ linear	ϵ	$\tau_{span}\|_{0.90}$ parabolic	ϵ
10	0.624	0.610	0.609	-0.25%	0.607	-0.49%
15	0.630	0.607	0.616	+1.37%	0.608	+0.12%
20	0.594	0.588	0.581	-1.27%	0.588	-0.09%
25	0.530	0.522	0.519	-0.52%	0.522	+0.12%
30	0.460	0.449	0.452	+0.72%	0.448	-0.23%

Table 4.5 Comparison between the experimental measurement and the results of the 4.6 in terms of K_{span} for $\eta = 0.8$.

$\delta_{r_{ref}}$ (deg)	τ_{ref}	experimental measurement	$\tau_{span}\|_{0.80}$ linear	ϵ	$\tau_{span}\|_{0.80}$ parabolic	ϵ
10	0.624	0.600	0.594	-0.99%	0.597	-0.53%
15	0.630	0.587	0.591	+0.66%	0.587	-0.01%
20	0.594	0.547	0.547	+0.04%	0.548	+0.15%
25	0.530	0.471	0.481	+2.05%	0.472	+0.22%
30	0.460	0.418	0.411	-1.68%	0.412	-1.34%

4.5 Aerodynamic Interference

The aerodynamic interference among airplane components is evaluated by the ratio of aerodynamic coefficients between two configurations, which differ for only one component. Figure 4.25 shows the effects of fuselage, wing, and horizontal tail on the vertical tail on a given aircraft configuration (high wing, body-mounted horizontal), at several angles of sideslip and for two rudder deflection 0° and 10°. It can be observed that the addition of the aircraft components changes the slope and translates the curves, except for the wing contribution, which is negligible. Linearity is conserved up to 12° of sideslip at $Re = 470000$. The aerodynamic interference due to the local sideslip angle induced by the rudder deflection is apparent at zero sideslip angle, where the leap from 0° to 10° of rudder deflection between the curves of the same configurations is different. This confirms the results presented in [13].

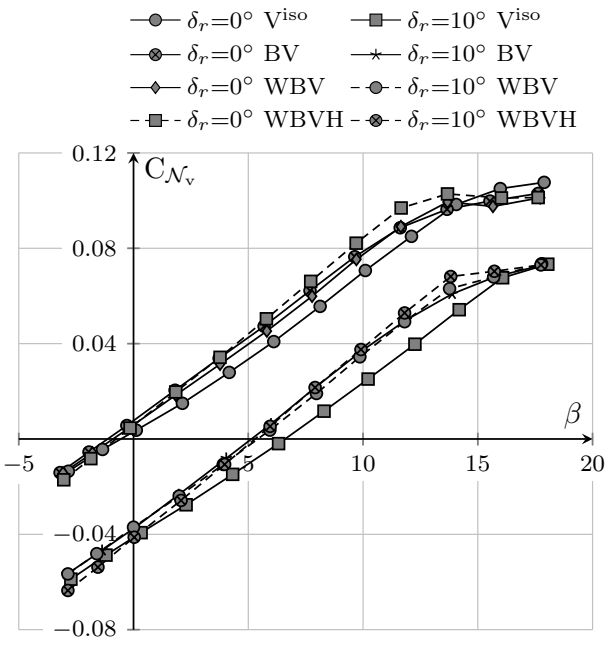

Figure 4.25 Effects of rudder deflections on vertical tail yawing moment coefficient in several configurations at different angles of sideslip at $Re = 470000$.

Coefficients can be defined to isolate the contribution of each component. For instance the effect of the fuselage on the vertical tail contribution to the control power derivative is given by the ratio $K_{B_v} = C_{\mathcal{N}_{v_{\delta_r}}}$ (BV) / $C_{\mathcal{N}_{v_{\delta_r}}}$ (V), where B stands for body and V stands for vertical tailplane. Similarly K_{W_v} and K_{H_v} are the coefficients that give the effect of the wing and the horizontal tail respectively on the vertical tail contribution to $C_{\mathcal{N}_{v_{\delta_r}}}$, thus the global effect can be obtained by

multiplying these factors. The general ratio K is defined such that

$$K \begin{cases} < 1, & \text{the aerodynamic interference } \textit{decreases } \mathrm{C}_{\mathcal{N}_{\mathrm{v}_{\delta_r}}}, \\ = 1, & \text{the aerodynamic interference } \textit{does not affect } \mathrm{C}_{\mathcal{N}_{\mathrm{v}_{\delta_r}}}, \\ > 1, & \text{the aerodynamic interference } \textit{increase } \mathrm{C}_{\mathcal{N}_{\mathrm{v}_{\delta_r}}}. \end{cases}$$

As stated in the equation 4.2 the yawing moment coefficient can be split into two parts, both of which can be evaluated through a surrogate model that account for aerodynamic. The study about the yawing moment coefficient derivative respect to the sidesplip angle, $\mathrm{C}_{\mathcal{N}_\beta}$, was in depth analyzed in Ciliberti's work [6]. As regards the control power derivative here follows an analysis based upon the wind tunnel tests campaign conducted in this work. It can be stated that the main contribution to the control power derivative is given by the vertical tail and can be calculated as follows

$$C_{\mathcal{N}_{\mathrm{v}_{\delta_r}}} = K_{\mathrm{B_v}} K_{\mathrm{W_v}} K_{\mathrm{H_v}} C^{\text{isolated}}_{\mathcal{N}_{\mathrm{v}_{\delta_r}}} \tag{4.18}$$

where $\mathrm{C}^{\text{isolated}}_{\mathcal{N}_{\mathrm{v}_{\delta_r}}}$ is the control power derivative of the isolated vertical tail, which in a preliminary formulation can be defined as

$$C^{\text{isolated}}_{\mathcal{N}_{\delta_r}} = \frac{dC_{\mathcal{N}}}{d\delta_r} = -a_v \tau_v V_v \eta_v \tag{1.31}$$

the τ_v term can be calculated, for istance, by mean of the method introduced in the Section 4.4.

It should be noted that the acquired data relating to the assembly *A* have been obtained with a slightly different mounting of the tailplane inside the fuselage tail-cone with respect to the data acquired by the assemblies *B* and *C*.

This defect in the mounting caused a different systematic error in the data of the three assemblies and therefore the interference coefficients were constructed depending on the rudder fraction chord ($\mathrm{K}_i = \{ (\mathrm{c}_r/\mathrm{c})$), i.e. they have not been normalized with respect to this parameter.

4.5.1 Body - vertical tail interference factor $\mathrm{K}_{\mathrm{B_v}}$

The interference factor $\mathrm{K}_{\mathrm{B_v}}$ is defined as the ratio between the yawing moment coefficient of the fuselage - vertical tail combination to the yawing moment coefficient of the isolated vertical tailplane

$$K_{\mathrm{B_v}} = \frac{C_{\mathcal{N}_{\mathrm{v}_{\delta_r}}}(BV)}{C_{\mathcal{N}_{\mathrm{v}_{\delta_r}}}(V)} \tag{4.19}$$

Figures 4.26 and 4.27 represent the effect of the fuselage on the vertical tailplane in terms of control power, three curves have been plotted according to the rudder's fraction chord c_r/c for both the aspect ratios. *The overall fuselage effect is a slight decrease of the vertical tail control power ($K_{\mathrm{B_v}} < 1$)*, in particular this effect is less

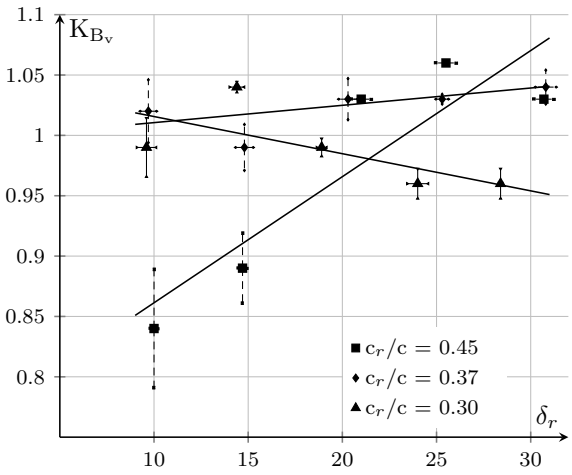

Figure 4.26 Interference factor K_{B_v} vs rudder deflection δ_r - All assemblies, $\mathcal{AR}$ = 1.5.

remarkable for the shorter aspect ratio, where the values tend to be closer to the unit and in some cases exceed this value. Drawning the linear trend lines for each (c_r/c,$\mathcal{AR}$), it can be seen that the effect of the fuselage tend to reduce itself with the increasing of the rudder deflection, thus for high values of δ_r $K_{B_v} \geq 1$ in almost every case, showing that *for high values of the rudder deflection the fuselage effect increases the vertical tail control power* (the only curve that shows a different trend is the one relative to (c_r=0.3/c,$\mathcal{AR}$=1.5)).

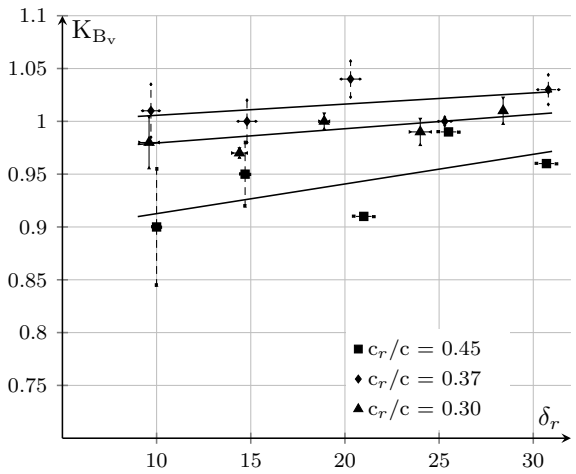

Figure 4.27 Interference factor K_{B_v} vs rudder deflection δ_r - All assemblies, *AR* = 2.0 full span.

4.5.2 Wing - vertical tail interference factor K_{W_v}

The wing interference factor K_{W_v} is defined as the ratio between the yawing moment coefficient of the wing - fuselage - vertical tail combination to the yawing moment coefficient of the fuselage - vertical tailplane combination and represents the effect due to the fall of dynamic pressure that arises on the vertical tail in an aircraft that have a fuselage with a small wake effect, like the one used in this test campaign.

$$K_{W_v} = \frac{C_{\mathcal{N}_{v_{\delta_r}}}(WBV)}{C_{\mathcal{N}_{v_{\delta_r}}}(BV)} \tag{4.20}$$

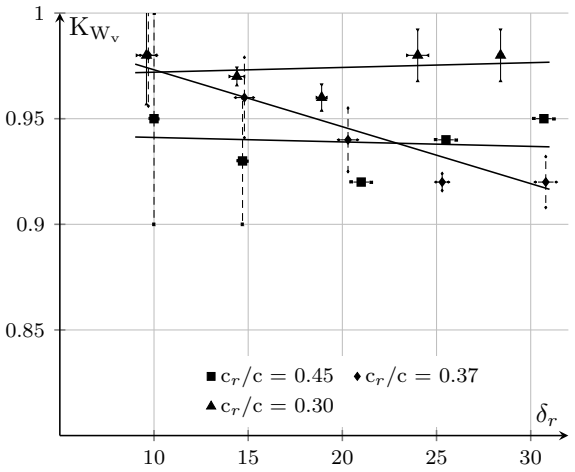

Figure 4.28 Interference factor K_{W_v} vs rudder deflection δ_r - All assemblies, AR = 1.5, high wing.

Figure 4.28 to 4.30 show the wing effect on the vertical tail control power, three curves have been plotted according to the rudder's fraction chord c_r/c for both the aspect ratios in the configuration with high wing, while only two of them where analyzed in the configuration with low wing only for the shorter aspect ratio. *The overall effect of the wing is a decrease of the vertical tail control power ($K_{W_v} < 1$)*, in particular the configurations with high wing show a stronger effect, up to $5-6\%$ of reduction for the high wing against $2-3\%$ for the low wing. The change in aspect ratio, for the configuration with high wing, show a tendency to reduce the wing effect: the K_{W_v} coefficient tends to be closer to the unit value and to exceed it in some points. The linear trend lines show an almost constant behaviour (or a decrescent trend for some (c_r/c,AR)) in function of the rudder deflection, thus *the wing effect remains pejorative for the full range of δ_r.*

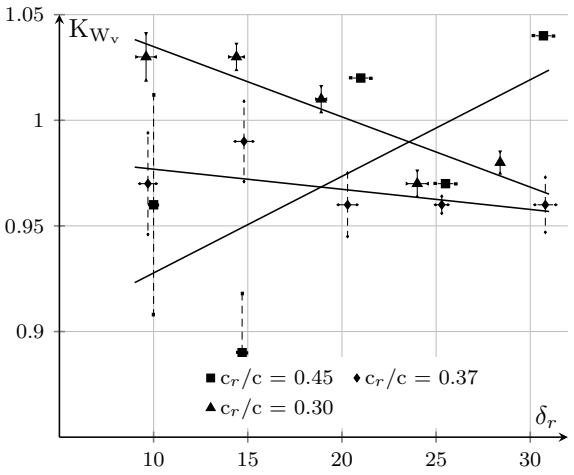

Figure 4.29 Interference factor K_{W_v} vs rudder deflection δ_r - All assemblies, AR = 2.0 full span, high wing.

4.5.3 Horizontal - vertical tail interference factor K_{H_v}

The horizontal tail interference factor K_{H_v} is defined as the ratio between the yawing moment coefficient of the wing - fuselage - horizontal tail - vertical tail combination to the yawing moment coefficient of the wing - fuselage - vertical tailplane combination

$$K_{H_v} = \frac{C_{\mathcal{N}_{v_{\delta_r}}}(WBVH)}{C_{\mathcal{N}_{v_{\delta_r}}}(WBV)} \tag{4.21}$$

Two positions of the horizontal tailplane were tested: the body-mounted con-

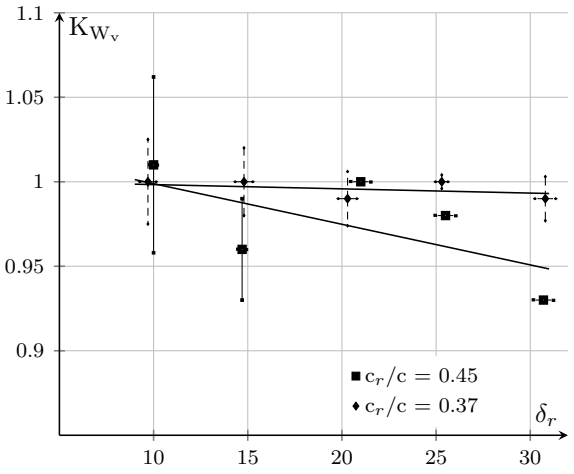

Figure 4.30 Interference factor K_{W_v} vs rudder deflection δ_r - Assemblies A and B, AR = 1.5, low wing.

figuration (which will be referred to as $H1$) was analyzed for all the assemblies, while the T-tail configuration (which will be referred to as $H5$) was provided only for assemblies B and C.

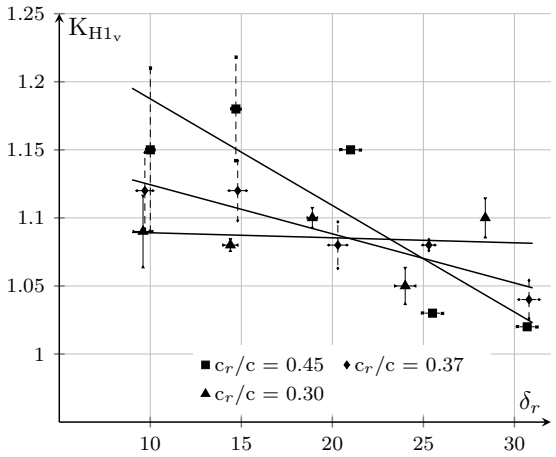

Figure 4.31 Interference factor K_{H1_v} vs rudder deflection δ_r - All assemblies, AR = 1.5, high wing.

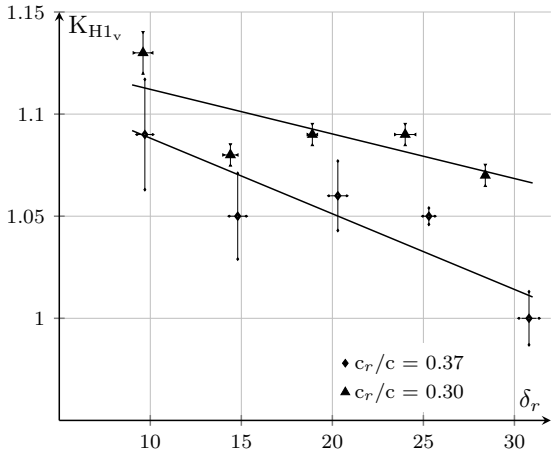

Figure 4.32 Interference factor K_{H1_v} vs rudder deflection δ_r - Assemblies B and C, AR = 2.0 full span, high wing.

Figures 4.31 and 4.32 show the interference factor for the body-mounted horizontail tail configurations, Figures 4.33 and 4.34 for the T-tail. In each configuration analyzed the general trend line gives always a K > 1, thus *there is an increase of the rudder control power provided by the horizontal tailplane mounted in its most external positions*. This effect is more intense than the previous ones, for istance the increment on the directional control derivatives for low angles of rudder deflection is from 8% up to 20%. However it tends to reduce itself with the increasing of

the rudder deflection, as can be seen from the linear trend lines drawn, *the effect of the horizontal tail on the rudder control power decreases with the increase of the rudder deflection*. The T-tail configuration reaches higher values in terms of K_{H5_v} for each (c_r/c,ÆR), wherease the effect of the aspect ratio is different for each assembly: *B* shows lower values of K(δ_r), *C* shows higher values of K(δ_r) for both positioning of the horizontal tailplane.

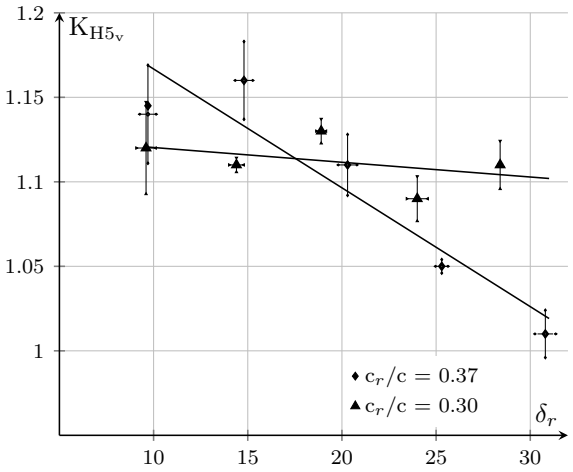

Figure 4.33 Interference factor K_{H5_v} vs rudder deflection δ_r - Assemblies *B* and *C*, ÆR = 1.5, high wing.

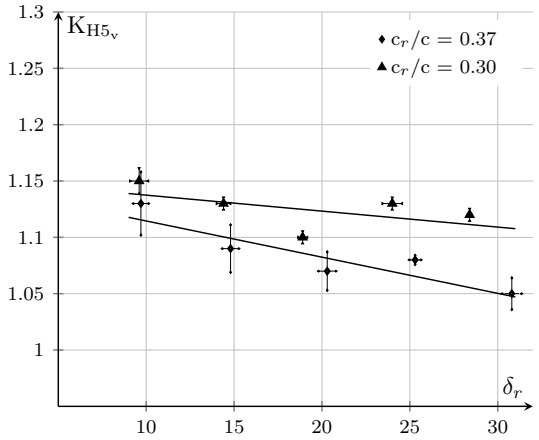

Figure 4.34 Interference factor K_{H5_v} vs rudder deflection δ_r - All assemblies, ÆR = 2.0 full span, high wing.

4.5.4 Superpositioning of the effects

Table 4.6 Results about the superpositioning of the effects in the calculation of the interference factors.

δ_r		AR= 1.5				AR= 2.0		
(deg)	K'$_{W_C}$	ϵ_W	K'$_{H1_C}$	ϵ_{H1}	K'$_{W_C}$	ϵ_W	K'$_{H1_C}$	ϵ_{H1}
10	0.98	+0.03%	1.09	-0.03%	1.03	-0.64%	1.13	+0.64%
15	0.99	+2.17%	1.06	-2.13%	1.03	-2.96%	1.08	+3.06%
20	0.99	+2.66%	1.07	-2.59%	1.01	-0.40%	1.08	+0.40%
25	1.00	+1.65%	1.04	-1.62%	0.97	+1.90%	1.09	-1.87%
30	1.04	+6.30%	1.04	-5.93%	0.98	+0.76%	1.07	-0.75%

To ensure the superpositioning of the effects, two set of tests were performed with a partial configuration `BH_H1_C_E100` for both aspect ratios. The interference coefficients of the wing and of the body-mounted horizontal tailplane were calculated once again using the above mentioned configuration.K'$_{W_C}$ and K'$_{H1_v}$ were determined as

$$K'_{W_C} = \frac{C_{N_{C_{\delta_r}}}(WBVH1)}{C_{N_{C_{\delta_r}}}(BVH1)} \tag{4.22}$$

$$K'_{H1_C} = \frac{C_{N_{C_{\delta_r}}}(BVH1)}{C_{N_{C_{\delta_r}}}(BV)} \tag{4.23}$$

Table 4.6 resumes the results of the comparison between the interference factors defined before and the new ones here introducted. The superposition is ensured for both the coefficient and aspect ratios, in particular the slender tail shows a better agreement (lower values of error ϵ, which is calculated as K'/K) than the shorter one due to the more intense three-dimensional effects.

4.6 A method for the calculation of the rudder control power

Once the aerodyamic interference factors are introduced, a method can be defined to evaluate the rudder control power by mean of the equation presented in the Section 4.5 and here repeated

$$C_{\mathcal{N}_{v_{\delta_r}}} = K_{B_v} K_{W_v} K_{H_v} C^{\text{isolated}}_{\mathcal{N}_{v_{\delta_r}}} \tag{4.18}$$

$$C^{\text{isolated}}_{\mathcal{N}_{\delta_r}} = \frac{dC_{\mathcal{N}}}{d\delta_r} = -a_v V_v \eta_v \; \tau_v^{\text{isolated}} \tag{1.31}$$

where the first three parameters depend on the geometry of the vertical tail. The lift curve slope of the isolated vertical tail a_v can be calculated with Helmbold-Diederich formula

$$a_v = C_{L_{\alpha\, v}} = \frac{2\pi \mathcal{AR}}{2 + \sqrt{\mathcal{AR}^2 \frac{B^2}{\kappa^2}\left(1 + \frac{\tan^2 \Lambda_{v,c/2}}{B^2}\right) + 4}} \tag{4.24}$$

where

B is the compressibility parameter, $\sqrt{1 - M^2}$;

κ is the ratio of *section* lift-curve slope to theoretical thin-section value, $C_{l_\alpha}/(2\pi B)$, and for thin airfoils ($C_{l_\alpha} \simeq 2\pi$) it is equal to $1/B$;

$\Lambda_{v,c/2}$ is the vertical tail sweep angle at half chord.

A first application of the method is here given for the generic regional turboprop used in the wind tunnel test campaign. It is here noted that the configurations involved in this validation have not been directly use to derive the method. Different calculations have been made to evaluate the $C_{\mathcal{N}_{v_{\delta_r}}}$ for partial and total aircraft configurations. In addition, by mean of the method introduced in the Section 4.4 for the evaluation of the effectiveness, it was possible to evaluate the control power for each assembly.

To calculate the rudder control power of the configuration `BH_WH_H5_C_V20_E100`, the K factors relative to that chord ratio must be used

$$C^{\texttt{BH\_WH\_H5\_C\_V20\_E100}}_{\mathcal{N}_{C_{\delta_r}}} = C^{\text{isolated}}_{\mathcal{N}_{C_{\delta_r}}} * K_{B_C} K_{W_C} K_{H5_C} \tag{4.25}$$

where the subscript C of each coefficient means that they are evaluated on the curve relative to $c_r/c = 0.30$. The directional control derivative of the isolated vertical tail is calculated as

$$C^{\text{isolated}}_{\mathcal{N}_{C_{\delta_r}}} = -a_v V_v \eta_v * \tau_C^{\text{isolated}} \tag{4.26}$$

where $\eta_v = 0.9$, $V_v = 0.174$ from Table 2.1, and a_v is calculated by mean of the 4.24 assuming $M = 0$, airfoil $C_{l_\alpha} = 2\pi$, and $\Lambda_{v,c/2} = 17.98°$; these three parameters are the same for each assembly.

$$\tau_C^{\text{isolated}} = \tau_B^{\text{isolated}} * K_{\text{chord}} \tag{4.27}$$

Table 4.7 Comparison between the experimental measurement and the results of the 4.26 and 4.25.

$\delta_{r_{\text{ref}}}$	$C^{\text{isolated}}_{\mathcal{N}_{v_{\delta_r}}}$			$C^{\texttt{BH\_WH\_H5\_C\_V20\_E100}}_{\mathcal{N}_{v_{\delta_r}}}$		
(deg)	experimental	evaluated	ϵ	experimental	evaluated	ϵ
10	-0.0036	-0.0037	+0.88%	-0.0043	-0.0043	-0.67%
15	-0.0037	-0.0037	-1.73%	-0.0042	-0.0041	-1.21%
20	-0.0035	-0.0034	-1.75%	-0.0039	-0.0038	-0.81%
25	-0.0031	-0.0032	+2.80%	-0.0034	-0.0036	+3.77%
30	-0.0027	-0.0027	-0.55%	-0.0030	-0.0029	-2.84%

$\delta_{r_{\text{ref}}}$	$C^{BH\_WL\_H1\_V15\_A\_E100}_{\mathcal{N}_{v_{\delta_r}}}$		
(deg)	exp.	evaluated	ϵ
10	-0.0035	-0.0034	-1.72%
15	-0.0036	-0.0036	+2.98%
20	-0.0036	-0.0033	-6.52%
25	-0.0032	-0.0031	-3.89%
30	-0.0026	-0.0027	+4.33%

Table 4.8 Comparison between the experimental measurement and method results for the configuration `BH_WL_H1_V15_A_E100`.

$\delta_{r_{\text{ref}}}$	$C^{\texttt{BH\_WH\_V20\_B\_E80}}_{\mathcal{N}_{v_{\delta_r}}}$		
(deg)	exp.	evaluated	ϵ
10	-0.0040	-0.0041	+2.68%
15	-0.0039	-0.0039	+0.83%
20	-0.0036	-0.0036	+0.05%
25	-0.0031	-0.0032	+2.83%
30	-0.0027	-0.0027	-3.11%

Table 4.9 Comparison between the experimental measurement and method results for the configuration `BH_WH_V20_B_E80`.

the values of τ_C^{isolated} where already been calculated and reported in Table 4.3.

Table 4.7 shows the results of the calculation. Tables 4.8 and 4.9 report the results for the configurations `BH_WL_H1_V15_A_E100` and `BH_WH_V20_B_E80` respectively.

4.7 A preliminary design application: vertical tail sizing to minimum control speed

Minimum control speed V_{MC} is the calibrated airspeed, at which, when the critical engine is suddenly made inoperative, it is possible to maintain control of the airplane with that engine still inoperative, and maintain straight flight with an angle of bank of not more than 5° [14]. The *airborne* minimum control speed may not exceed 1.13 times the reference stall speed, hence *it affects the take-off field length*, which must be kept as low as possible, otherwise payload could be reduced on short runways. In one engine inoperative (OEI) condition, the vertical tail must counteract the airplane asymmetrical thrust. Forces and moments acting on the airplane in OEI conditions are shown in Figure 4.35, whereas a preliminary vertical tail surface sizing can be outlined with the chart shown in Figure 4.36. The propeller-driven engine generates a thrust which decreases with airspeed, while the yawing moment of the vertical tail may be expressed as stated in Section 1.3

$$\mathcal{N}_v = \frac{1}{2}\rho V^2 S b C_{\mathcal{N}_{\delta_r}} \delta_r \tag{4.28}$$

$$C_{\mathcal{N}_{\delta_r}} = a_v V_v \eta_v \tau_r \tag{4.29}$$

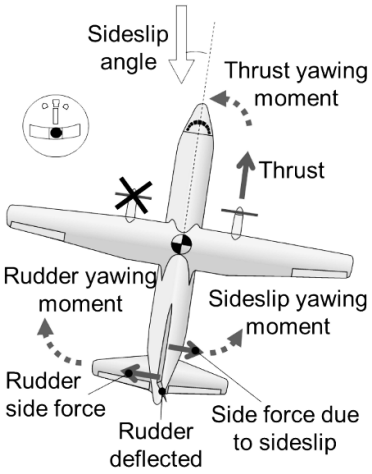

Figure 4.35 Moments acting in OEI conditions.

For a regional turboprop aircraft, with $\mathcal{AR}$= 2.0, c_r/c = 0.37, η = 0.90, S_v = 14.7 m^2, Figure 4.36 shows the intersection of the curves due to the engine yawing moment (straight line) and the yawing moment generated by the rudder deflection, which is proportional to the square of the airspeed, calculated with different methods, to keep the aircraft in directional equilibrium at a small sideslip angle. The intersection of the curves determines the airborne minimum control speed. It is apparent that the effect of an increasing planform area (or rudder

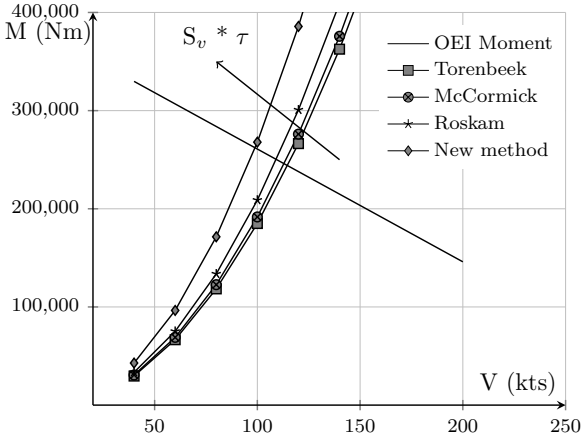

Figure 4.36 Vertical tail sizing plot: Moments vs minimum control speed, V_{MC}.

efficiency) is to reduce the minimum control speed. For the given tail planform, semi-empirical methods provide a rudder efficiency at high rudder deflection from 20% to 30% lower, which corresponds to an increase of V_{MC} from 10% to 15%, with respect to the result provided by the new method , Figure 4.37.

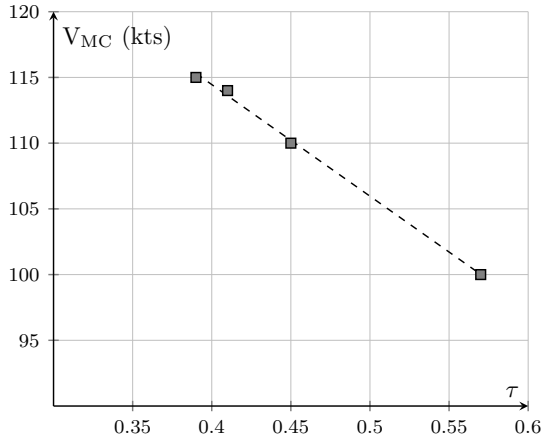

Figure 4.37 Effect of the rudder efficiency on V_{MC} for a given planform area.

Alternatively, for a given V_{MC}, dictated by the airplane take-off stall speed, the rudder efficiency affects the vertical tail planform area. For the same aircraft, assuming V_{MC} = 110 kts, an increase of 30% in rudder efficiency corresponds to a decrease of planform area up to 45%, Figure 4.38. The tailplane structural weight is directly proportional to the planform area [15], hence the weight reduction follows the same trend, Figure 4.36. With weight, drag and costs decrease. If, for any reason, i.e. directional stability issues, the tail area is fixed, a higher rudder efficiency may lead to a reduced control surface area and, consequently, a smaller actuator size, saving in weight and costs.

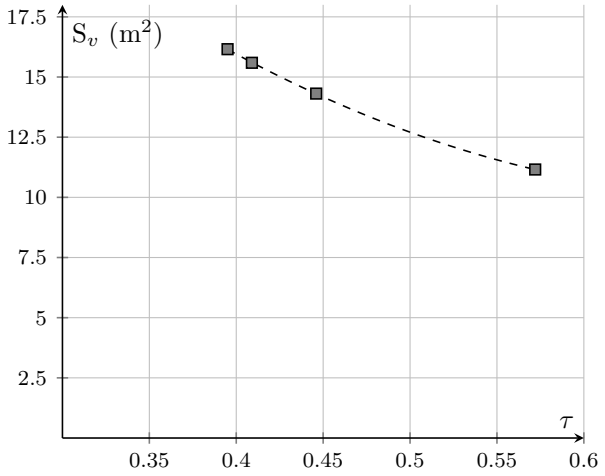

Figure 4.38 Effect of the rudder efficiency on the vertical tail area for a given V_{MC}.

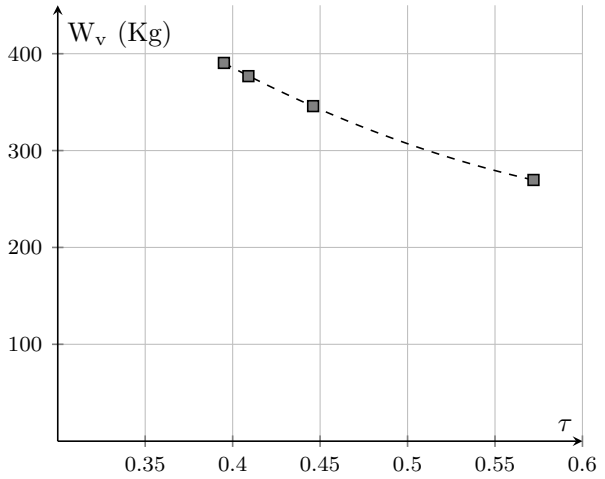

Figure 4.39 Effect of the rudder efficiency on the vertical tail mass for a given V_{MC}.

Chapter 5

Conclusion

This thesis presented a wind tunnel investigation of a control surface for wing with short aspect ratio, focusing on the estimation of the effectiveness τ of a vertical tail's rudder for the directional control of a generic regional transport airplane and to provide data about the aerdynamic interference among aircraft components. Vertical tail plane's design necessarily passes through the determination of the control derivatives and the more accurate the latter, the better the former. At time of writing, several semi-empirical methods exist for the determination of the rudder effectiveness, which have the great advantage of being quickly applied and easy to understand, but at the same time involve great disadvantages that land to an incorrect estimation of the effectiveness and thus an erroneous sizing of the vertical tail.

The first chapter has introduced the directional aerodynamics of an airplane in sideslip conditions (β>0), focusing on the contribution to the directional stability and control for the sizing of the vertical tailplane surface.

The second chapter has described the vertical tail assemblies involved in the wind tunnel test campaign in all their components, while the third chapter presented the main subsonic wind tunnel facility of the Department of Industrial Engineering (DII) and all the set-up procedures involved in the campaign.

The fourth chapter reported all the results of the experimental investigation. The effectiveness of the rudder is analyzed as function of different geometrical parameters (fraction of rudder chord, aspect ratio, rudder span) and a method for its evaluation is introducted to have a better estimation in a preliminary design phase. Then the aerodynamic interference among airplane subparts, calculated as the ratio between directional control derivatives of aircraft configurations differing for one component, was evaluated and implemened in a method for the estimation of the rudder control power $C_{\mathcal{N}_{\delta_r}}$. These new methods were validated by comparing them with the wind tunnel data acquired in the test campaign and compared to the semi-empirical methods for the estimation of the minimum control speed v_{MC}.

The result of this work is of considerable interest, since it provides results that agree with recent numerical and experimental analyses on regional and general

aviation airplanes ([3], [6], [12]).

Future works are to be conducted to investigate on other effects (i.e. airfoil's leading edge shape) and adding more aircraft configurations, eventually with the support of numerical analysis that can be validated by mean of the experimental results highlighted in this thesis.

Appendix A

CAD Drawnings

The following drawnings of the CAD model are reported:

1. Assembly *A* - *AR* = 1.5, Figure A.1;
2. assembly *A* - *AR* = 2.0, Figure A.2;
3. assembly *B* - *AR* = 1.5, Figure A.3;
4. assembly *B* - *AR* = 2.0, Figure A.4;
5. assembly *C* - *AR* = 1.5, Figure A.5;
6. assembly *C* - *AR* = 2.0, Figure A.6;
7. the common base, Figure A.7;
8. the hinge of the rudder, Figure A.8.

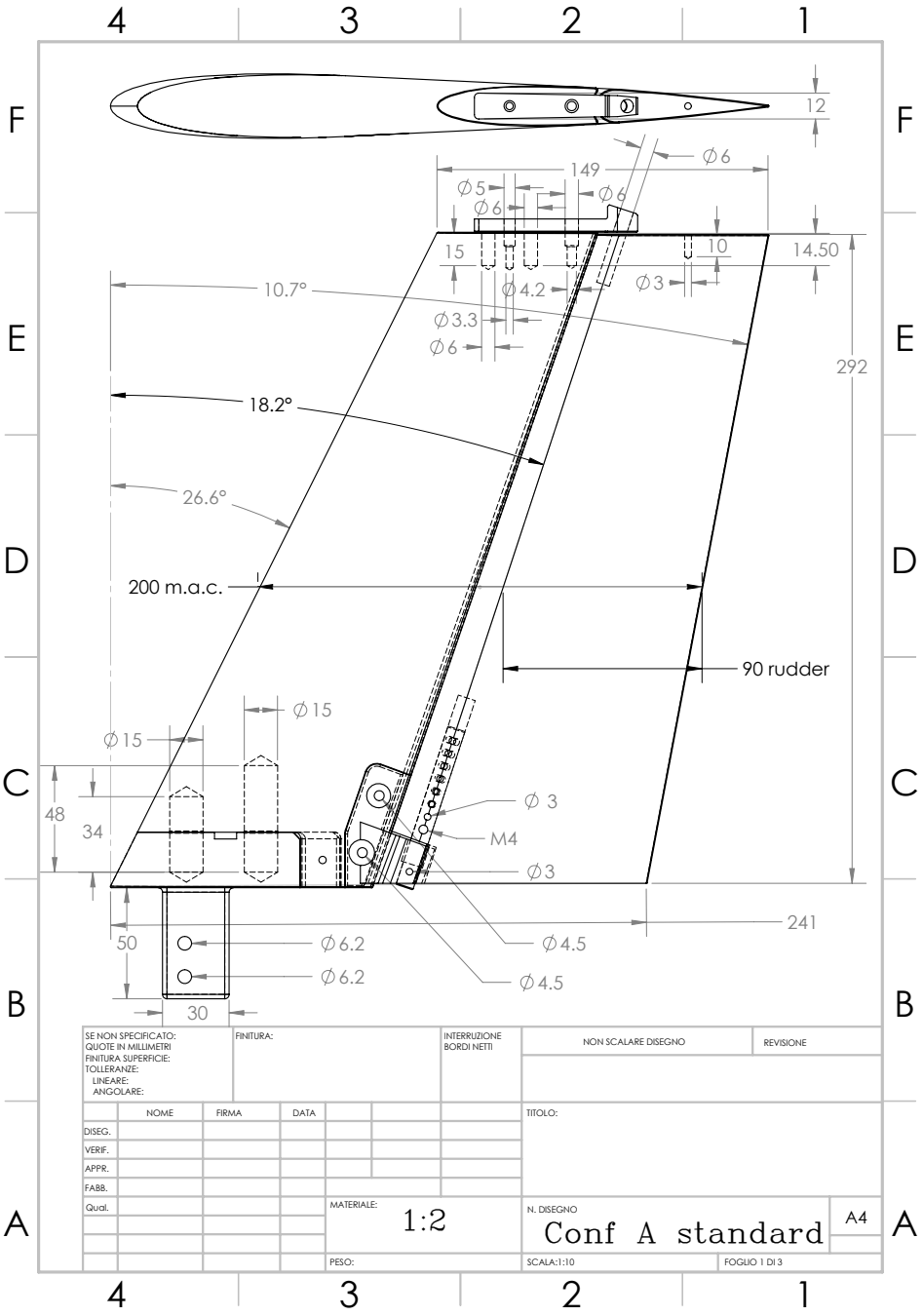

Figure A.1 CAD model of tail assembly *A* with *A*R = 1.5.

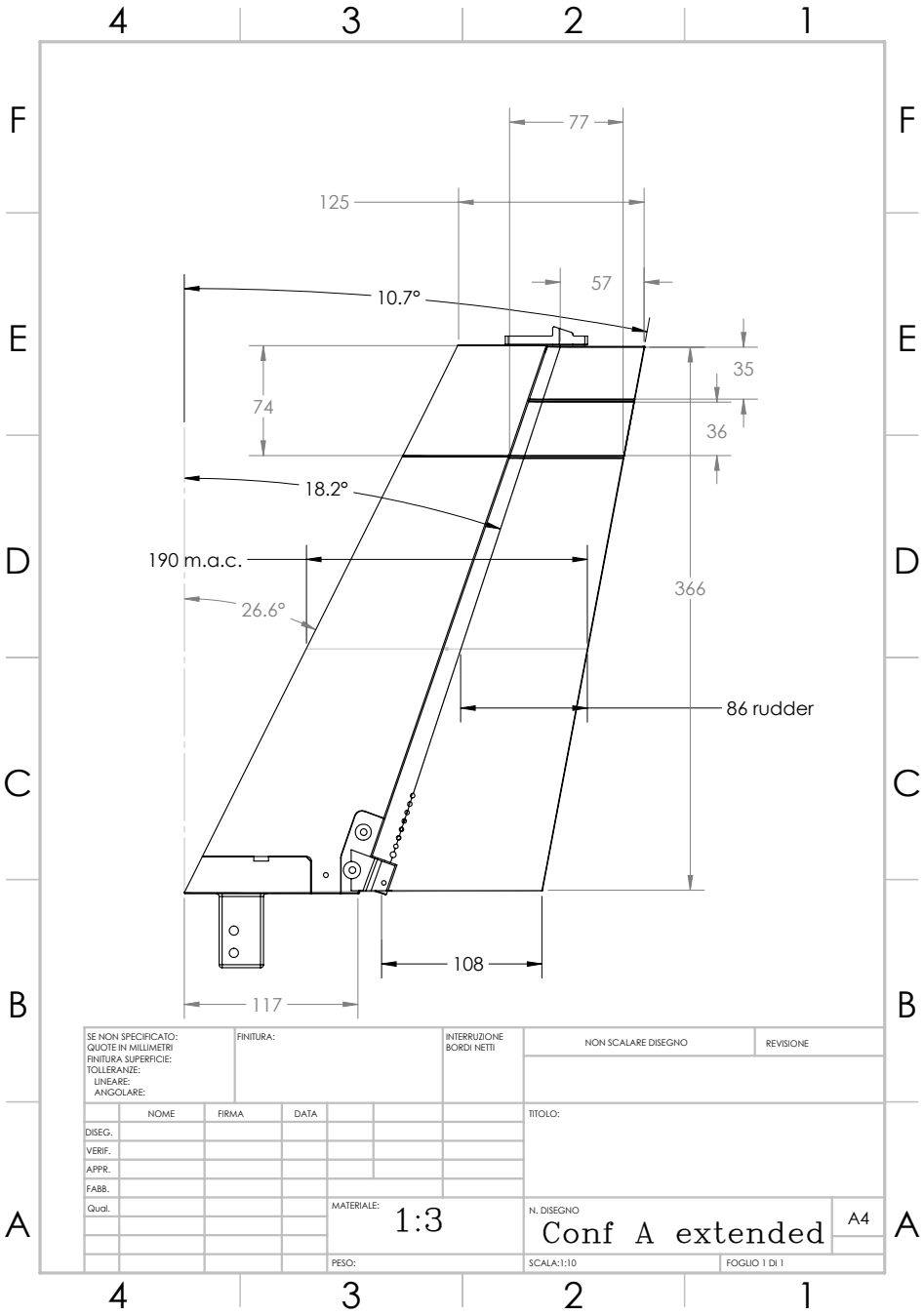

Figure A.2 CAD model of tail assembly *A* with $\mathcal{A}\mathbf{R}$ = 2.0.

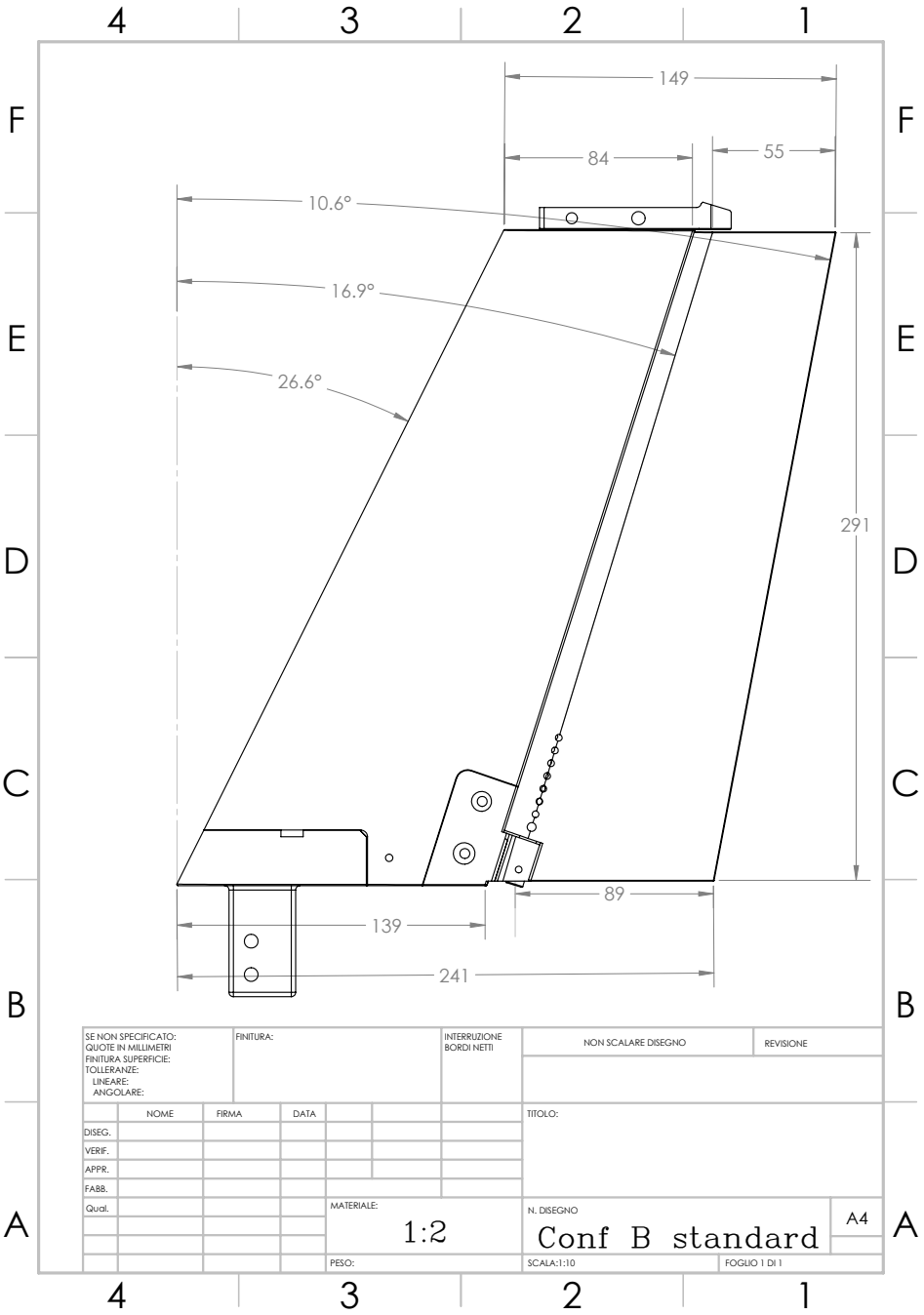

Figure A.3 CAD model of tail assembly *B* with *A*R = 1.5.

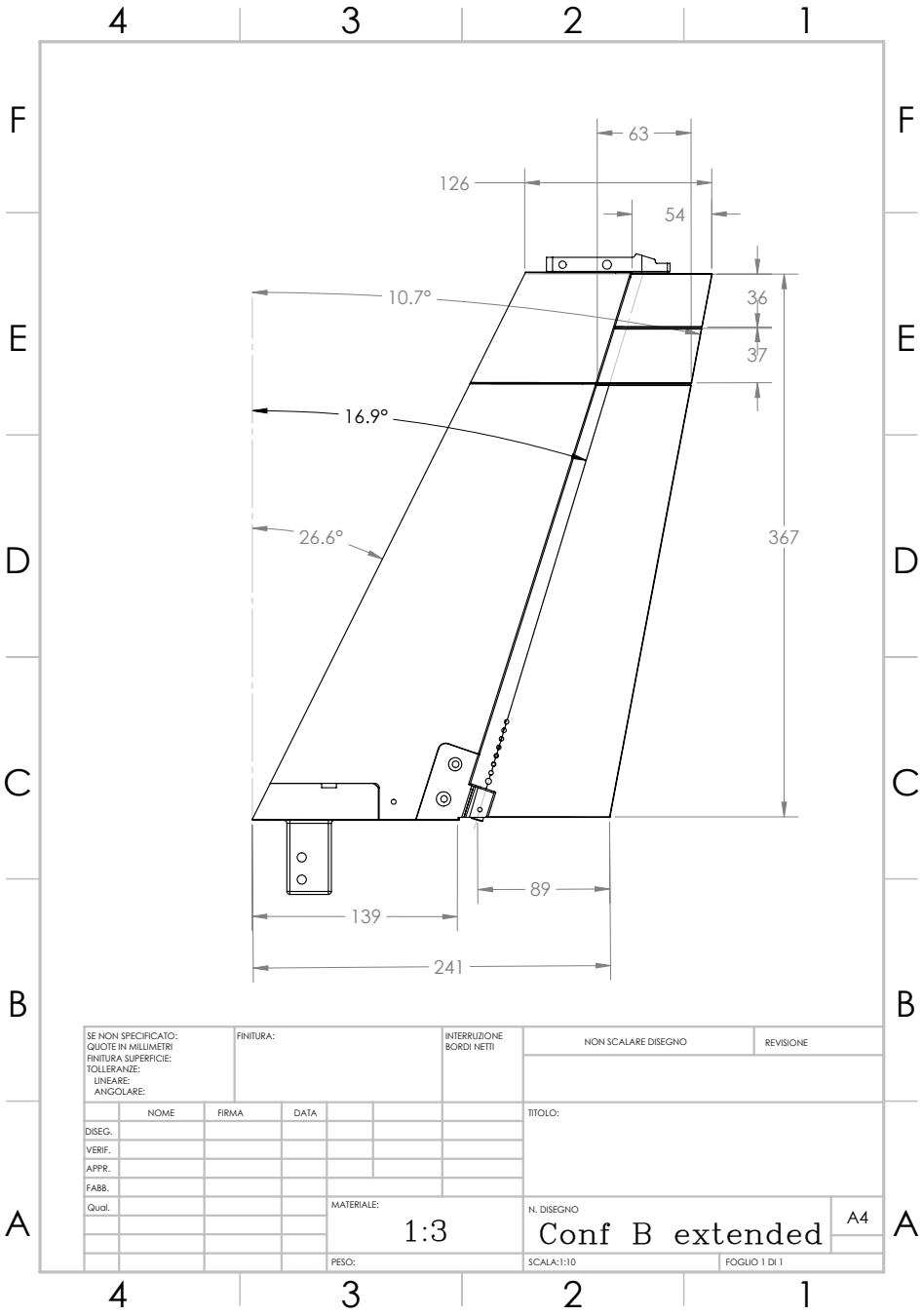

Figure A.4 CAD model of tail assembly *B* with *Æ*R = 2.0.

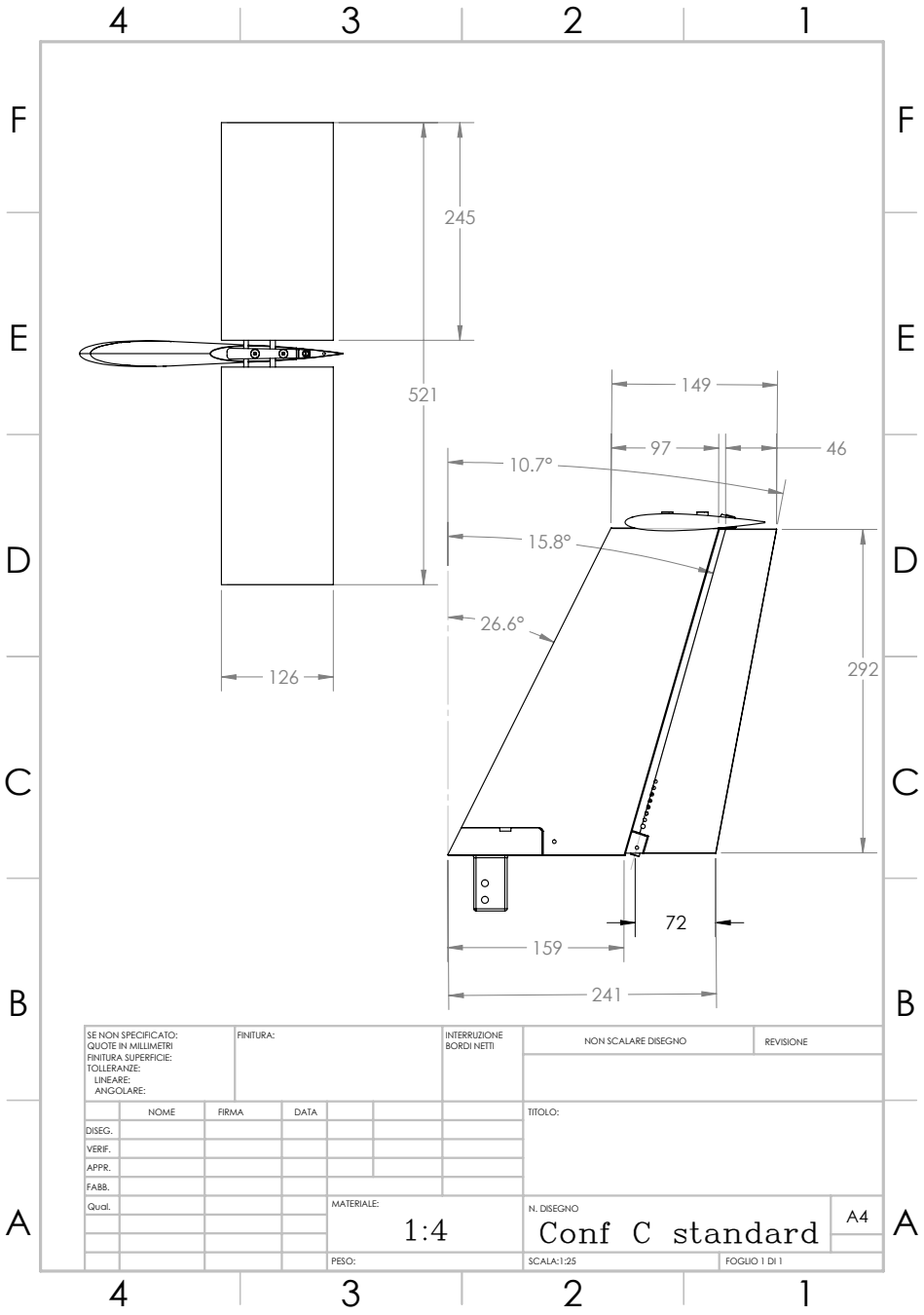

Figure A.5 CAD model of tail assembly *C* with $\mathcal{R}$ = 1.5.

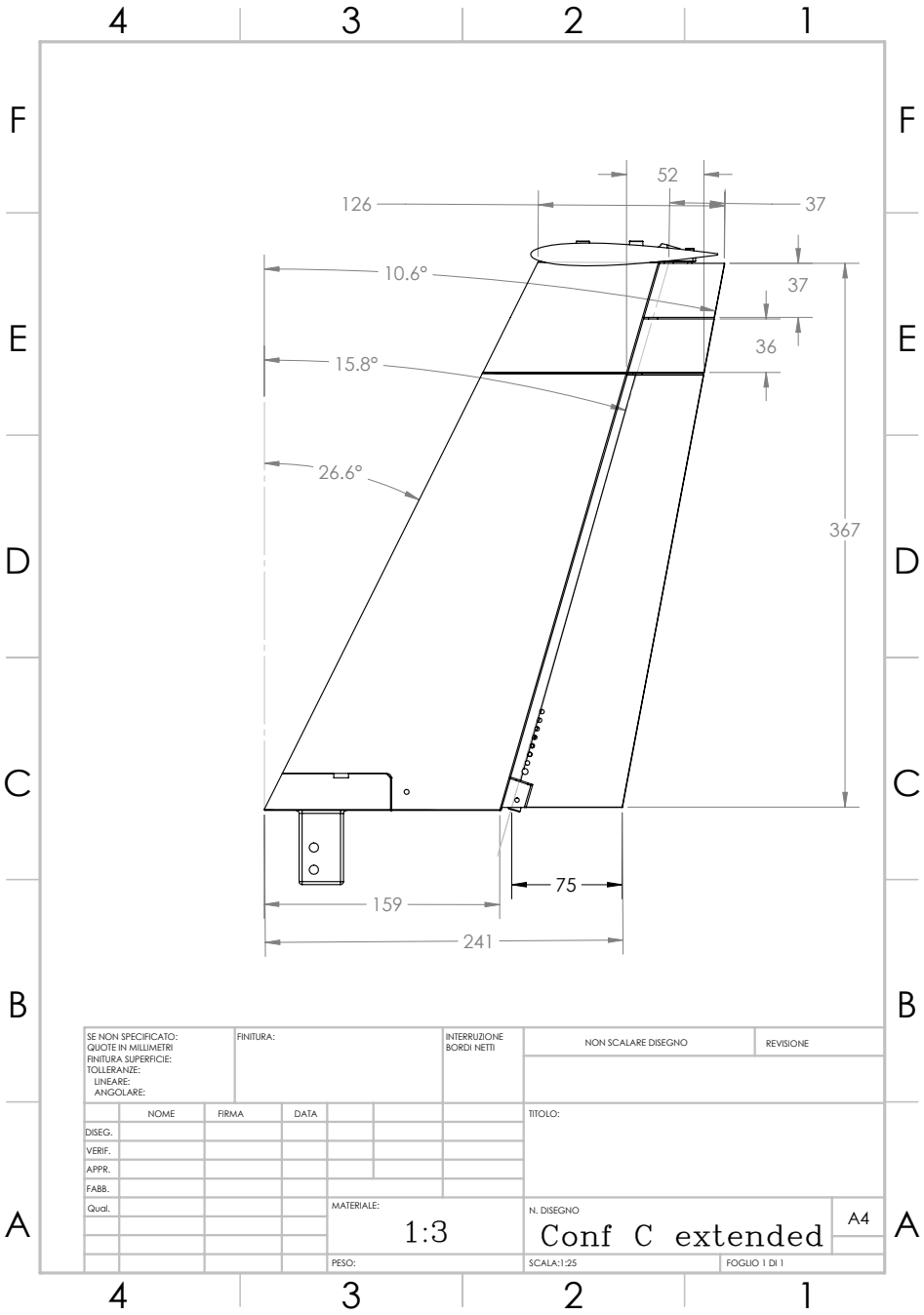

Figure A.6 CAD model of tail assembly *C* with *A*R = 2.0.

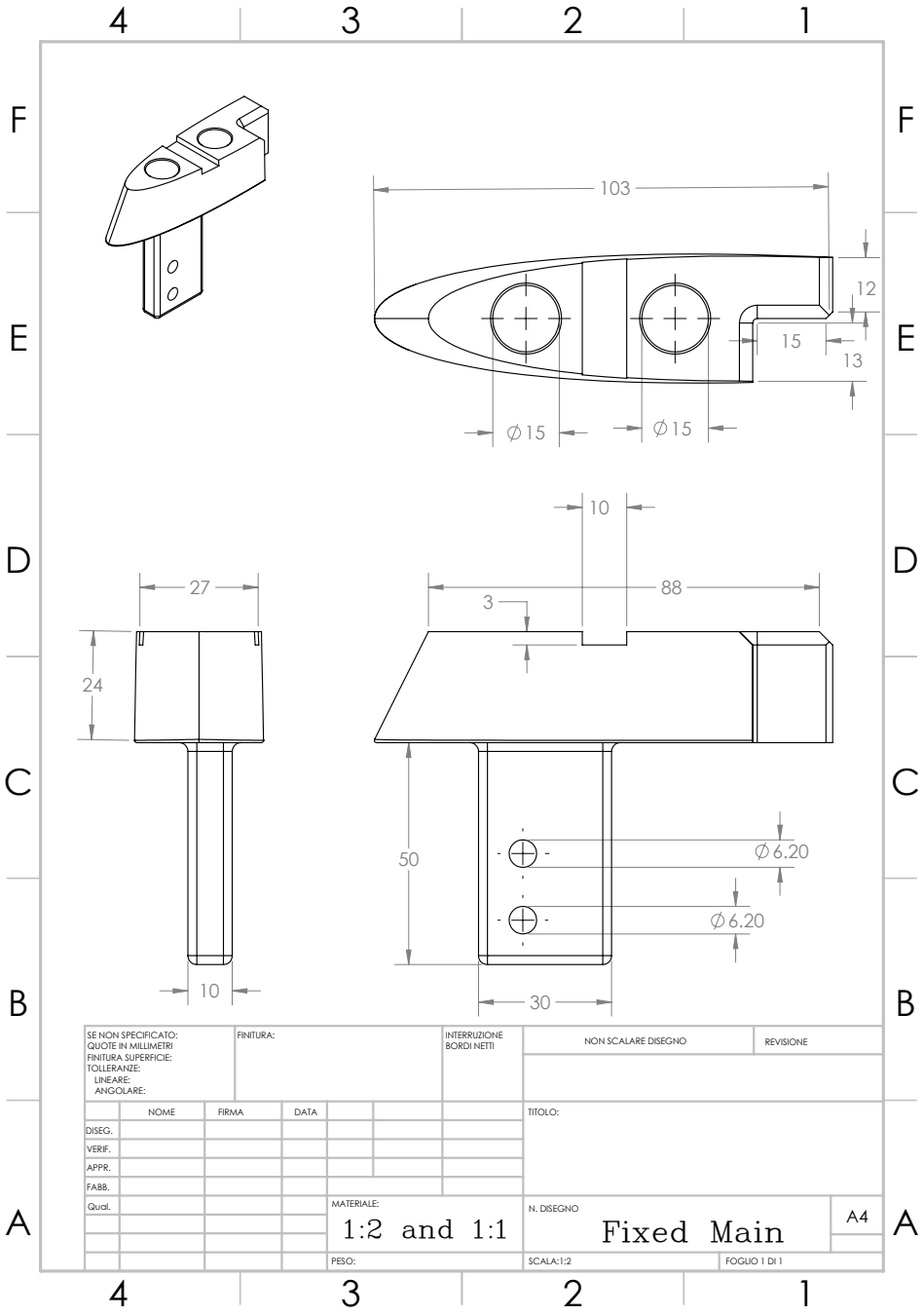

Figure A.7 CAD model of the common base.

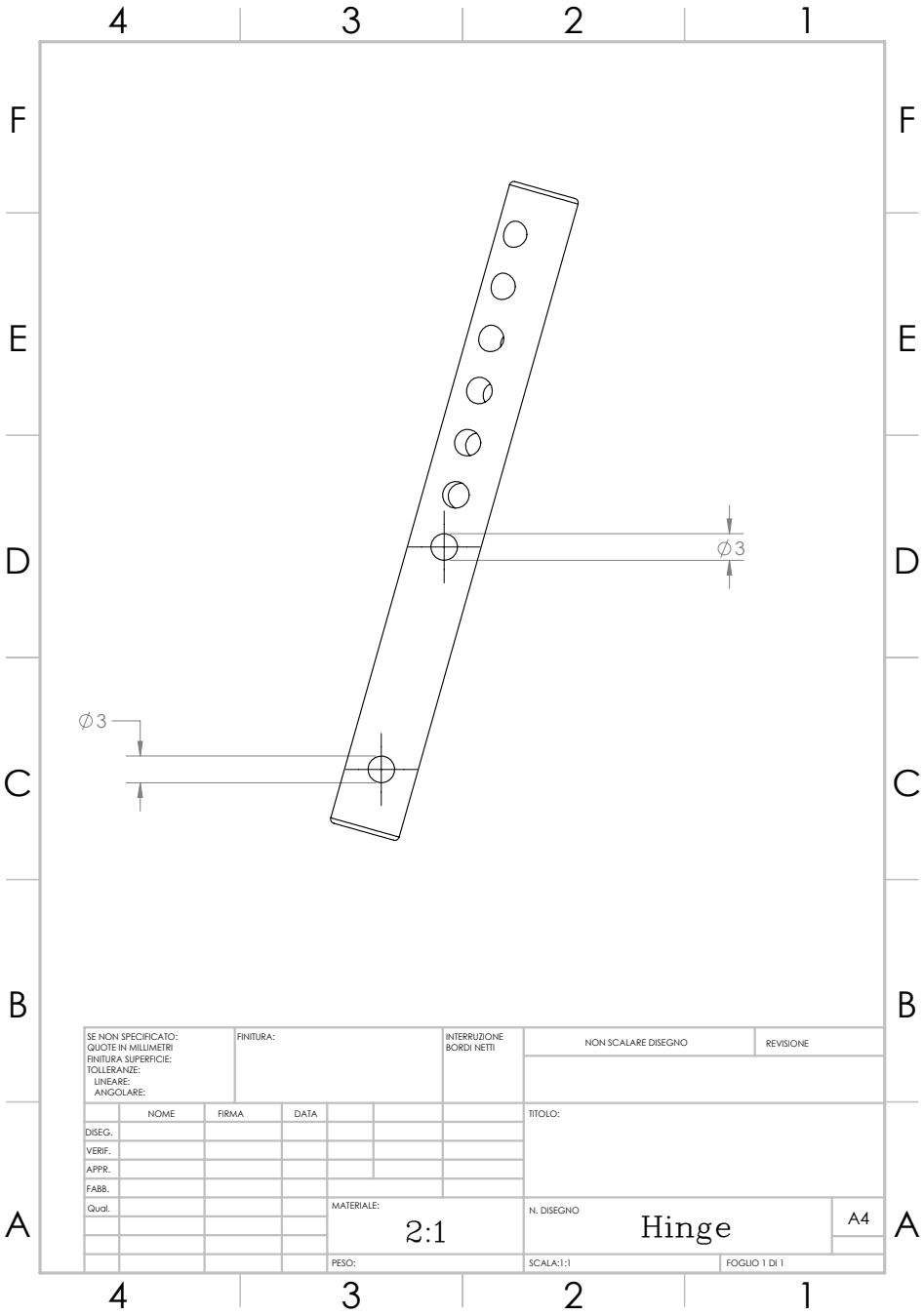

Figure A.8 CAD model of the hinge around witch the rudder rotates.

Bibliography

[1] C. D. Perkins and R. E. Hage. *Airplane performance stability and control*. New York: Wiley, 1949.

[2] *Aerodynamic Design Guidelines of Aircraft Dorsal Fin*. 34th AIAA Applied Aerodynamics Conference. AIAA AVIATION Forum, AIAA 2016-4330.

[3] Pierluigi et al. Della Vecchia. "P2012 WT test report".

[4] I. Kroo and J. Alonso. *Tail design and sizing*. Stanford University, 2012.

[5] E et al. Obert. *Aerodynamic design of transport aircraft*. Amsterdam, The Netherlands: Ios Press, 2009.

[6] Danilo Ciliberti. "An improved preliminary design methodology for aircraft directional stability prediction and vertical tailplane sizing". PhD thesis. UniversitÃ degli Studi di Napoli "Federico II", 2016.

[7] S. Corcione. "Design Guidelines, Experimental Investigation and numerical Analysis of a New Twin Engine Commuter Aircraft". PhD thesis. Universitá degli Studi di Napoli "Federico II", 2015.

[8] J. B. Barlow, W. H. Rea, and A. Pope. *Low-speed wind tunnel testing*. 3rd. New York: Wiley, 1999.

[9] Barnes Warnock McCormick. *Aerodynamics, Aeronautica, and Flight Mechanics*. New York: Wiley, 1995.

[10] Jan Roskam. *Airplane Design*. Lawrence, Kan: DAR corporatio, 1997.

[11] Egbert Torenbeek. *Synthesis of Subsonic Airplane Design: An Introduction to the Preliminary Design of Subsonic General Aviation and Transport Aircraft, with Emphasis on Layout, Aerodynamic Design, Propulsion and Performance*. Delft: Delft University Press, 1976.

[12] Ciro Scalzo. "Aircraft directional control characteristics through CDF analyses". MA thesis. Universitá degli Studi di Napoli "Federico II", 2015.

[13] Fabrizio Nicolosi, Pierluigi Della Vecchia, and Danilo Ciliberti. "Aerodynamic interference issues in aircraft directional control". In: *Journal of Aerospace Engineering* (June 2014).

[14] EASA. *Acceptable Means of Compliance for Large Aeroplanes CS-25*. European Aviation Safety Agency, 2015.

[15] D. P. Raymer. *Aircraft design: a conceptual approach. 5th edition.* Reston, VA: American Institute of Aeronautics and Astronautics, 2012.